https://doi.org/10.5194/hess-2022-31
Preprint. Discussion started: 10 March 2022

Hydrology and Earth System Sciences
Discussions
Open Access
EGU

Numerical modeling of physical and biochemical processes in the subsurface and their impacts on the self-potential signature

Xin Liu, Zengyu Zhang, Alex Furman

Faculty of Civil and Environmental Engineering, Technion - Israel Institute of Technology, Haifa, 32000, Israel.

Corresponding to: Xin Liu (lucyliu0908@outlook.com) and Alex Furman (afurman@technion.ac.il)

https://doi.org/10.5194/hess-2022-31
Preprint. Discussion started: 10 March 2022

Hydrology and Earth System Sciences
Discussions
Open Access
EGU

Abstract

Subsurface contamination is a significant problem due to excessive fertigation and industrial and domestic wastewater discharge. With numerical modeling and geophysical tool development, subsurface contaminant research has become easier to implement and study. However, there is still a gap in coupling the biochemical processes and geophysical signals. Such a coupling model is needed to facilitate understanding subsurface processes and provide further theoretical basis to practice and field monitoring. Thus, this research aims to simulate the self-potential (SP) signature in response to physical and biochemical dynamics in the subsurface. For the physico-bio-chemical model, the processes of water flow, solute transport, biochemical reactions, microbial dynamics, adsorption, and gas flow are considered. Specifically, the biochemical cycles related to C, N, Mn, Fe, and S are incorporated in the model. The physico-bio-chemical model is then coupled with the SP model. The SP model is addressed by Poisson's continuity equation, based on streaming and redox potential contribution. The streaming potential is calculated by the effective excess charge density and the water flow velocity, while the Butler-Volmer equation solves the redox potential. The results show that redox processes dominate the SP signals. Oxygen and nitrate concentrations present positive relationships with redox potential and dominate the redox potential in the oxic and anoxic environment, respectively. Nitrification and dissolved organic carbon (DOC) aerobic oxidation rates show positive relationships with redox potential. In contrast, the denitrification rate presents a negative relationship. The higher reaction rates for different redox processes also correspond to their optimal redox potential ranges. The streaming potential affected by water content and flux contributes little to SP, and the negative values along with soil depth become less remarkable. Generally, the SP and redox potential model can better reflect redox species concentrations and reaction rates, while the streaming potential model can reflect the water content and flux dynamics. Thus, the research can guide the detection of redox-sensitive contamination and water leakage in the subsurface.

1 Introduction

Subsurface contamination caused by anthropogenic activities is a widespread problem. It can be attributed to various reasons, such as pesticide, herbicide and fertilizer applications, industrial and domestic wastewater discharge, etc. To study the physical and biochemical dynamics in the subsurface, experimental measurement and numerical modeling on contaminant fate and transport

https://doi.org/10.5194/hess-2022-31
Preprint. Discussion started: 10 March 2022


Hydrology and Earth System Sciences
Discussions

are usually implemented. Moreover, with the advantage of being minimally invasive and of relatively low cost, geophysical methods have also become an emerging set of tools for subsurface monitoring, such as direct current electrical conductivity, self-potential (SP), and induced polarization.

Self-potential (SP) is a passive geophysical method to measure the natural electrical potential distribution of the earth. The SP survey does not require the application of an external electric current. The potential differences are generated by the small, naturally induced currents that occur in the subsurface, recorded by a set of non-polarizing electrodes, typically at the earth's surface (Revil et al., 2009; Soueid Ahmed et al., 2020). Such naturally induced currents are attributed to electrical charge uneven distributions or electron transfer resulting from water flux or biochemical redox processes (Linde and Revil, 2007). Moreover, the signature is affected by the subsurface hydraulic and electrical properties (Hu et al., 2020). Thus, when combined with hydrological and biogeochemical processes, the SP technique can be specifically used to localize and quantify water flow (e.g., pumping test and water leakage) (Oliveti and Cardarelli, 2017) and redox-sensitive contaminant distribution (e.g., metallic and organic matter) (Revil et al., 2009; Forté and Bentley, 2013) and estimate soil hydraulic and electrical properties (e.g., hydraulic and electrical conductivity) (Jouniaux et al., 2020).

SP signature induced by water flow is defined as streaming potential. It occurs when a hydraulic potential gradient drives an electrolyte through a channel or pore with charged walls (Lyklema, 1995; Li, 2004) (Fig. 1 (b)). Along the water flux direction, electrical charges move downstream driven by the hydraulic potential gradient (i.e., carried by water flow), generating convection current in the porous media (Möckel et al., 1998). At narrow bottlenecks, where the electrical double layers of two grains overlap, charges may also accumulate. As the head gradient (pressure in horizontal systems) is the source driving force of steaming potential, streaming current density was previously formulated by the hydraulic potential gradient multiplying by a streaming current coupling coefficient (Sill, 1983). This traditional formulation has been proven to be useful and was applied to numerous hydrological investigations (Santos et al., 2002; Allègre et al., 2012; DesRoches and Butler, 2016). However, the direct process that derives the streaming currents is the water flow. Hence, the classic formulation, that does not consider the permeability, makes it difficult to extend to unsaturated conditions (Bolève et al., 2007). As a more intuitive phenomenon of streaming potential generation results from uneven charge distribution, driven by water flow,

https://doi.org/10.5194/hess-2022-31
Preprint. Discussion started: 10 March 2022

Hydrology and Earth System Sciences
Discussions

later, a formulation that directly links streaming current density to water flow velocity and effective excess charge density was developed (Bolève et al., 2007). This formulation is suitable to model streaming potential in the field, as been widely applied to hydrological studies. Examples include pumping tests (Soueid Ahmed et al., 2016), seepages from ditches or into sinkholes (Bolève et al., 2007), water leakage in dams (Bolève et al., 2011; Soueid Ahmed et al., 2020), or contaminated site affected by hydrological dynamics (Abbas et al., 2017). Moreover, the formulation was also extended to the inertial laminar flow regime and unsaturated area with excellent agreement between the theory and experimental data (Jardani et al., 2007; Mboh et al., 2012; Soueid Ahmed et al., 2019), making it more applicable to vadose zone research (Soldi et al., 2020).

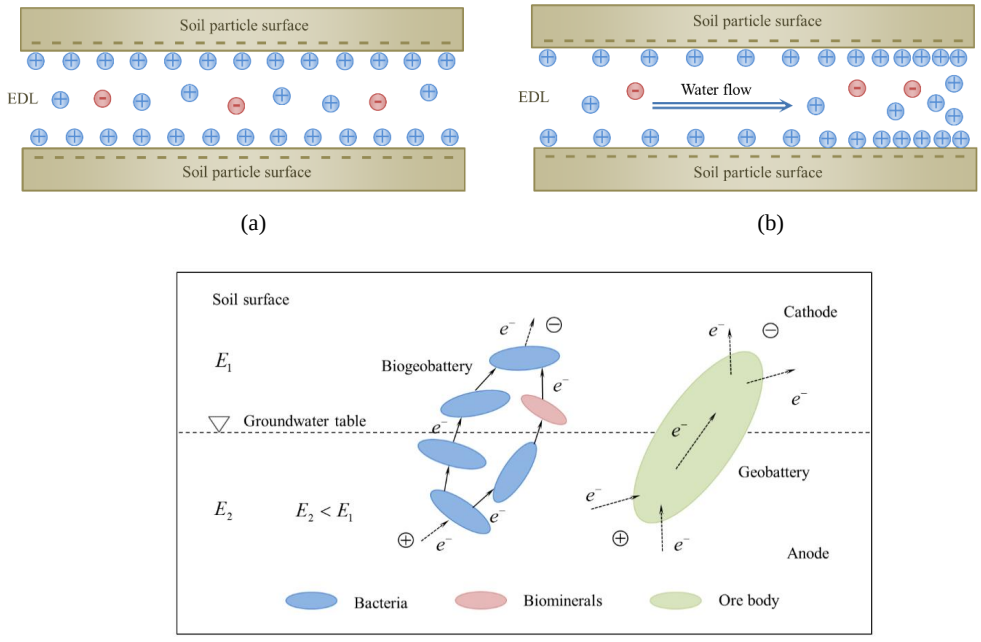

Figure 1 Schematic of streaming and redox potential induced by physical and biochemical processes. Panes (a) and (b) illustrate electrical charge distributions in a static state and induced by water flow, respectively. Pane (c) illustrates electron transfer caused by redox processes (modified based on Jouniaux et al.(2009) and Revil et al. (2010)). EDL is the abbreviation for electrical double layer.

SP associated with redox processes is induced by electron transfer, where electron donors (e.g., organic carbon) deliver electrons to acceptors (e.g., oxygen or nitrate) driven by redox potential (Jouniaux et al., 2009). In addition, the electrons can transfer through the bacterial

https://doi.org/10.5194/hess-2022-31
Preprint. Discussion started: 10 March 2022


Hydrology and Earth System Sciences
Discussions

extracellular appendages (also known as nanowires) as well as biominerals formed by microbial activities (Arora et al., 2007; Jouniaux et al., 2009). This process, where electrons transfer from anode to cathode (Fig. 1(c)) is similar to that of a 'geobattery', in which electrons transfer through the ore body (Revil et al., 2010; Fernandez et al., 2019). In such cases, the SP anomaly associated with redox processes is induced in the surrounding conductive media (Castermant et al., 2008). Thus, the redox potential and SP associated with redox processes can reflect biochemical degradation. These are increasingly applied to experimental and field studies, such as estimating carbon, nitrogen, and phosphorus removal by redox potential data (Yu et al., 1997) and detecting ionic and organic contaminant plumes by SP technique (Revil et al., 2009; Forté and Bentley, 2013; Cui et al., 2017; Fernandez et al., 2019). With software development, numerical modeling becomes a more available and cost-effective method to study SP contributed by redox potential. The Nernst equation is a widely used method to calculate the potential of redox couples (e.g., H_2O/O_2, CH_4/CO_2, NH_4^+/NO_3^-, NO_2^-/NO_3^-, $Fe^{2+}/Fe(OH)_3$, H_2S/SO_4^{2-}, $As(III)/As(V)$) in thermodynamic equilibrium reactions (Schüring et al., 2000) However, Meyer et al. (2014) showed that the Nernst equation is unsuitable for all redox couples as numerous biochemical processes are characterized by a kinetic state in a natural environment (rather than equilibrium). The Butler-Volmer equation (Butler, 1924a, 1924b, 1932; Erdey-Grúz and Volmer, 1930) was adopted to address this issue. The Butler-Volmer equation describes how the electrical currents pass through an electrode in a redox kinetic state and generate a voltage difference in the bulk electrolyte (Dickinson and Wain, 2020). This can better reflect the process of redox potential measurement (Schüring et al., 2000) and is more suitable for redox potential modeling. Early research mainly focused on parameter verification and sensitivity analyses (Tanaka and Tamamushi, 1964; Peiffer et al., 1992). In recent studies, the Butler-Volmer equation was usually combined with a model of the relevant biochemical process, which was used to analyze the relationship between substrate concentration and redox potential (Picioreanu et al., 2007; Hamelers et al., 2011; Zhao et al., 2016; Jin et al., 2020). However, there is a gap in using the Butler-Volmer concept to calculate redox potential for complex kinetic reactions and analyze the signature in response to biochemical dynamics on temporal and spatial scales.

Based on the very limited research of simulating the SP signature and its forming processes, the objectives of this study are (1) to set up a physico-bio-chemical model that would couple the processes of water flow, solute transport, gas flow, biochemical reactions, microbial dynamics,

https://doi.org/10.5194/hess-2022-31
Preprint. Discussion started: 10 March 2022


Hydrology and Earth System Sciences
Discussions

and adsorption in the soil system; (2) to establish an SP model by considering the contribution of streaming potential (related to water flux and effective excess charge density) and redox potential (solved by Butler-Volmer Equation); (3) to couple the physico-bio-chemical and geophysical models, and to calibrate and verify the models using experimental data; (4) to apply the models to 90cm vertical soil column in which the capillary fringe underneath a soil aquifer treatment (SAT) site is modeled, and analyzed SP signals in response to subsurface water flow and biodegradation processes (mainly focusing on carbon and nitrogen transformation).

2 Model development

First, the model's soil physical and biochemical components (i.e., water flow, solute transport, gas flow, biochemical reactions, microbial dynamics, and equilibrium adsorption) are set up. Then, the SP model is established based on Poisson's continuity equation. Finally, the physico-bio-chemical and geophysical models are coupled by relating the physical and biochemical properties in the soil water system.

2.1 Physical and biochemical processes

In the physio-bio-chemical model, the Richards equation describes the water flow. The soil hydraulic properties are solved by the soil-hydraulic functions of van Genuchten-Mualem (van Genuchten, 1980). Multi-solute transport is simulated by the advection-dispersion equation, involving biochemical reactions, adsorption, and gas transfer as the sink/source terms. Biochemical reactions are described by multiple-Monod, second-order, and chemical equilibrium reactions. The adsorption is solved by the equilibrium between the concentrations in the aqueous phase and the soil surface. Finally, the advection-diffusion equation describes the gas flow, considering Henry's equilibrium law to address the transfer between aqueous and gas phases.

2.1.1 Water flow

The water flow is solved by the Richards equation, describing one-dimensional water movement in partially saturated porous media.

$$\frac{\partial \theta_w(h)}{\partial t} = \frac{\partial}{\partial z}\left[K(h)\left(\frac{\partial h}{\partial z} + 1\right)\right] \quad (1)$$

https://doi.org/10.5194/hess-2022-31
Preprint. Discussion started: 10 March 2022


Hydrology and Earth System Sciences
Discussions

where θ_w is the volumetric water content (-), h is the matric head (m), t is the time (s), z is the spatial coordinate (positive upward) (m), and K is the unsaturated hydraulic conductivity (m s^{-1}).

The unsaturated soil hydraulic properties, i.e., soil water content and unsaturated hydraulic conductivity, are in nonlinear functions of the pressure head. The model implements the soil hydraulic functions of van Genuchten (1980), who used the statistical pore size distribution model of Mualem (1976) to describe the unsaturated hydraulic conductivity function in terms of soil water retention parameters,

$$\theta_w(h) = \begin{cases} \theta_r + \dfrac{\theta_s - \theta_r}{\left[1+(\alpha h)^n\right]^m} & h < 0 \\ \theta_s & h \geq 0 \end{cases} \qquad m = 1-1/n,\ n>1 \tag{2}$$

$$K(h) = K_s S_e^l \left[1-\left(1-S_e^{1/m}\right)^m\right]^2 \qquad S_e = \frac{\theta_w - \theta_r}{\theta_s - \theta_r} \tag{3}$$

where θ_r is the residual water content (-), θ_s is the saturated water content (-), α, m, n are empirical parameters related to pore and grain size distribution, affecting the shape of hydraulic functions (m^{-1}), (-), (-), K_s is the saturated hydraulic conductivity (m s^{-1}), S_e is the effective saturation (-), and l is the pore connectivity parameter, often taken to be 0.5 (-).

2.1.2 Solute transport

The solute transport equation is derived from the advection-dispersion equation, considering the sink/source terms.

$$\frac{\partial \theta_w C_i}{\partial t} = \frac{\partial}{\partial z}\left(\theta_w D_i^w \frac{\partial C_i}{\partial z}\right) - \frac{\partial q_w C_i}{\partial z} + \theta_w s_{c,i} \tag{4}$$

where C_i is the concentration of species *i* in the aqueous phase (mol L^{-1}), D_i^w is the dispersion coefficient of species *i* in the aqueous phase (m^2 s^{-1}), q_w is the volumetric flux density (m s^{-1}), and $s_{c,i}$ is the sink/source term of species *i* in the aqueous phase (mol L^{-1} s^{-1}).

The dispersion coefficient in the aqueous phase, D_i^w is given by (Bear, 1972), with the tortuosity factors τ_w and τ_g for aqueous and gas phases (in Section 2.1.6) are the functions of the water and air contents and are described by the relationship of Millington and Quirk (1961),

https://doi.org/10.5194/hess-2022-31
Preprint. Discussion started: 10 March 2022


Hydrology and Earth System Sciences
Discussions

$$\theta_w D_i^w = D_L |q_w| + \theta_w D_{i,w} \tau_w \qquad \tau_w = \frac{\theta_w^{7/3}}{\theta_s^2} \tag{5}$$

where D_L is the longitudinal dispersivity (m), $D_{i,w}$ is the molecular diffusion coefficient of species *i* in free water (m^2 s^{-1}), and τ_w is the tortuosity factor in the aqueous phase (-).

The sink/source terms, involving biochemical reactions, adsorption (positive sign means desorption), and gas transfer, are presented as follows. The theory of each process will be further discussed in Sections 2.1.3, 2.1.5, and 2.1.6, respectively.

$$\theta_w s_{c,i} = \theta_w r_i + S_{ce,i} - S_i + \Gamma_i \tag{6}$$

where r_i is the total kinetic reaction rates that species *i* is involved (mol L^{-1} s^{-1}), $S_{ce,i}$ is the change of species *i* mass flux caused by chemical equilibrium reactions (mol dm^{-3} s^{-1}), such as complexation/hydrolysis and precipitation/dissolution, S_i is the adsorption change of species *i* attributed to the equilibrium with soil surface site density (mol dm^{-3} s^{-1}), and Γ_i is the gas transfer of species *i* addressd by Henry's equilibrium law (mol dm^{-3} s^{-1}).

2.1.3 Biochemical reactions

(1) Multiple-Monod kinetics

In multiple-Monod kinetics, it is assumed that the concentrations of all species involved in the reactions affect the biochemical processes (Molz et al., 1986). The multiple-Monod kinetics for the biochemical process *p* can be expressed as (Monod, 1949)

$$r^p = \mu_{\max}^p f_{\theta_w} X_m I_b(X_m) I_{nc}^p(C_i) \prod_i \left[\frac{C_i}{K_i^p + C_i} \right] \tag{7}$$

where r^p is the kinetic reaction rate for process *p* (mol L^{-1} s^{-1}), $\mu_{\max}^p$ is the maximum kinetic reaction rate for process *p* (mol C or N / g cell s^{-1}), f_{θ_w} is the reciprocal of θ_w (-), X_m is the biomass of bacteria *m* responsible for the reaction (g dm^{-3}), and K_i^p is the half-saturation constant of species *i* for reaction process *p* (mol L^{-1}).

In this research, the microbes are assumed to be retained in the soil, bacterial concentration (in the aqueous phase) is acquired by dividing the biomass by water content. $I_b(X_m)$ and $I_{nc}^p(C_i)$ are referred to as the biomass and non-competitive inhibition terms, expressed by follows (Segel, 1975; Kindred and Celia, 1989).

https://doi.org/10.5194/hess-2022-31
Preprint. Discussion started: 10 March 2022


Hydrology and Earth System Sciences
Discussions

$$I_b(X_m) = \left[\frac{k_{b,m}}{k_{b,m} + f_{\theta_w} X_m} \right] \quad (8)$$

$$I_{nc}^{p}(C_i) = \left[\frac{k_{I,C_i}^{p}}{k_{I,C_i}^{p} + C_i} \right] \quad (9)$$

where $k_{b,m}$ is the biomass inhibition constant (g L^{-1}), and k_{I,C_i}^{p} is the substrate inhibition constant for reaction process *p* (mol L^{-1}).

(2) Second-order reactions

In the natural environment, some chemical reactions related to soil substrate concentrations may occur spontaneously and are contributed less by microbial communities. In such a case, the second-order reaction is a more reasonable and easier method to solve the reaction instead of Monod kinetics. The second-order reactions in the model are considered to be proportional to the product of two reactant concentrations. The reaction rate for process *p* can be expressed as

$$r^p = k^p [C_1][C_2] \quad (10)$$

where k^p is the second-order reaction rate constant for process *p* (mol^{-1} L s^{-1}).

The total kinetic reaction rate for species *i* is equal to the sum of the rates for all processes in which the species *i* is involved, hence

$$r_i = \sum_p y_i^p r^p \quad (11)$$

where y_i^p is the specific coefficient of species *i* for reaction process *p* (-). When the species is the primary substrate, y_i^p is equal to 1. Otherwise, it is the ratio of species *i* relative to the primary substrate for reaction process *p*, as determined from stoichiometry.

(3) Chemical equilibrium reactions

Chemical equilibrium reactions, such as aqueous complexation/hydrolysis and precipitation/ dissolution, widely exist and affect biochemical processes in soil water systems. The equilibrium constants can be shown as

$$K_i^h = \frac{\prod_j C_j^{\gamma_j}}{C_i} \quad (12)$$

https://doi.org/10.5194/hess-2022-31
Preprint. Discussion started: 10 March 2022


Hydrology and Earth System Sciences
Discussions

$$K_i^{SP} = \prod_j C_j^{\gamma_j} \quad (13)$$

where K_i^h and K_i^{SP} are the equilibrium constants for species *i* complexation/hydrolysis and precipitation/dissolution, respectively, also known as hydrolysis equilibrium and solubility product constants, C_j is the concentration of specific *j* related to the chemical equilibrium reaction (mol L^{-1}), and γ_j is the stoichiometric coefficient of species *j* (-), a positive value means species *j* is on the opposite side to species *i* of the chemical equilibrium equation, while a negative value refers to on the same side.

2.1.4 Microbial dynamics

Microbial growth is assumed to be limited by Monod kinetics which the corresponding microbial community is involved in the reaction. The microbial dynamics is controlled by the microbial growth and death or maintenance rates, which is shown as

$$\frac{dX_m}{dt} = Y_m \theta_w r^p - X_m d_m \quad (14)$$

where Y_m is the microbial yield coefficient for bacteria *m* when mediating reaction process *p* (g cells / mol C or N), and d_m is the microbial death or maintenance rate constant for bacteria *m* (s^{-1}).

2.1.5 Adsorption

Equilibrium is considered between the concentrations in the aqueous phase and soil surface. The equilibrium constant is shown as

$$K_i^S = \frac{C_i X_\gamma}{C_i \cdot X^\gamma} \quad (15)$$

where K_i^S is the surface equilibrium constant for species *i* adsorption, X^- is the soil surface site density (mol L^{-1}), γ is the stoichiometric coefficient of soil surface site (-), $C_i X_\gamma$ is the surface complex concentration of species *i* (mol L^{-1}).

2.1.6 Gas flow

The advection-diffusion equation describes the gas flow, considering gas transfer (sink/source term of solute transport) between gas and aqueous phases.

https://doi.org/10.5194/hess-2022-31
Preprint. Discussion started: 10 March 2022


Hydrology and Earth System Sciences
Discussions

$$\frac{\partial \theta_g G_i}{\partial t} = \frac{\partial}{\partial z}\left(\theta_g D_i^g \frac{\partial G_i}{\partial z} \right) - \frac{\partial q_g G_i}{\partial z} - \Gamma_i \tag{16}$$

$$\theta_g D_i^g = \theta_g D_{i,g} \tau_g \qquad \tau_g = \frac{\theta_g^{7/3}}{\theta_s^2} \tag{17}$$

where G_i is the concentration of species *i* in the gas phase (mol cm^{-3}), θ_g is the volumetric gas content (-), D_i^g is the diffusion coefficient of species *i* in the gas phase (m^2 s^{-1}), q_g is the volumetric gas flux density (m s^{-1}), $D_{i,g}$ is the molecular diffusion coefficient of species *i* in the gas phase (m^2 s^{-1}), and τ_g is the tortuosity factor in the gas phase (-).

Henry's equilibrium law solves the gas transfer between the gas and aqueous phases. The equilibrium constant is shown as

$$K_i^H = \frac{C_i}{P_i} \tag{18}$$

where K_i^H are Henry's law constants of species *i* (mol L^{-1} atm^{-1}), and P_i is the partial pressure of species *i* in the gas phase (atm).

2.2 Self-potential

The SP distribution is attained by the solution to the following Poisson's equation.

$$\nabla \cdot (\sigma \nabla \varphi) = \nabla \cdot j_s \tag{19}$$

where σ is the electrical conductivity of porous media (S m^{-1}), φ is the self-potential (V), and j_s is the source current density (A m^{-2}).

In sandy soil, the surface conductivity can be ignored as it is much lower than the electrolyte conductivity (Duy Thanh et al., 2019). Based on Archie's law (Archie, 1942), the formulation of porous media conductivity is linked to the pore water conductivity, presented as

$$\sigma = \sigma_w \phi^m \tag{20}$$

$$\sigma_w = C_f N_A e \sum_{i=1}^{N} |z_i| \beta_i C_i \tag{21}$$

where σ is the pore water conductivity (S m^{-1}), ϕ is the connected porosity (-), m is the cementation exponent ($m = 1.645$) (Revil et al., 2012), e is the elementary charge ($e = 1.6 \times 10^{-19} C$), z_i is the valence of species *i*, β_i is the mobility of species *i* (m^2 s^{-1} V^{-1}), N_A is

https://doi.org/10.5194/hess-2022-31
Preprint. Discussion started: 10 March 2022


Hydrology and Earth System Sciences
Discussions

Avogadro's number ($N_A = 6.02\times10^{23}\,\mathrm{mol}^{-1}$), C_f is the constant ($C_f = 10^3$), and $C_f N_A$ is the unit conversion factor from mol L^{-1} to number m^{-3}.

When SP signals are induced by water flow and redox processes, occurring in a variably saturated environment, Eq. 19 can be written as

$$\nabla\cdot(\sigma s_w^n \nabla\varphi) = \nabla\cdot(j_{sc} + j_{rc}) \tag{22}$$

where s_w is the water saturation (-), n is the saturation exponent ($n = 1.98$) (Revil, 2013), j_{sc} is the streaming current density (A m^{-2}), and j_{rc} is the current density associated with redox processes (A m^{-2}).

The SP contributed by streaming and redox potential separately can be described as Eqs. 23 and 24, induced by water flow and redox processes, respectively.

$$\nabla\cdot(\sigma s_w^n \nabla\varphi_s) = \nabla\cdot j_{sc} \tag{23}$$

$$\nabla\cdot(\sigma s_w^n \nabla\varphi_r) = \nabla\cdot j_{rc} \tag{24}$$

where φ_s is the streaming potential (V), and φ_r is the SP associated with redox processes (V).

In the following, the formulations of streaming current density and current density associated with redox processes will be introduced explicitly in Sections 2.2.1 and 2.2.2. Then, SP, streaming potential, and SP associated with redox processes can be calculated based on Eqs. 22, 23, and 24, respectively.

2.2.1 Streaming potential

The electrolyte flow through porous media induces the streaming potential. The streaming current density equals the effective excess charge density per unit pore volume multiplying the water flow velocity. Considering saturation, the equation can be expressed as

$$j_{sc} = \frac{Q_v v}{s_w} \tag{25}$$

where Q_v is the effective excess charge density per unit pore volume dragged by water flow (C m^{-3}), and v is the water flow velocity (m s^{-1}).

Based on the observation by Jardani et al. (2007), the effective excess charge density is mainly related to the porous material permeability and the formulation is written as

$$Q_V = -9.2 - 0.82\log_{10}\kappa \tag{26}$$

https://doi.org/10.5194/hess-2022-31
Preprint. Discussion started: 10 March 2022


Hydrology and Earth System Sciences
Discussions

where κ is the permeability at saturation (m^2), and the relationship between permeability and saturated hydraulic conductivity is expressed as

$$\kappa = \frac{\eta_w K_s}{\rho_w g} \tag{27}$$

where η_w is the dynamic viscosity ($\eta_w = 9\times10^{-4}\,\mathrm{m^2\,s^{-1}}$), ρ_w is the water density ($\rho_w = 10^3\,\mathrm{kg\,m^{-3}}$), and g is the standard gravity ($g = 9.8\,\mathrm{m\,s^{-2}}$)

The water velocity is related to the volumetric flux through the water content, $v = \frac{q_w}{\theta_w}$, which can be simulated by coupling with the water flow model (Eqs. 1-3).

2.2.2 Redox potential

The current density contributed by redox processes is associated with the redox potential gradient, formulated as

$$j_{rc} = -\sigma s_w^n \nabla E \tag{28}$$

where E is the redox potential (V).

To calculate the redox potential, we assume the redox reaction for a single redox couple *j* is presented as

$$\mathrm{Ox}_j + n_j e^- \rightleftharpoons \mathrm{Red}_j \tag{29}$$

where n_j is the number of electron transfer per molecule oxidized or reduced, Ox_j is the oxidized species (electron acceptors), and Red_j is the reduced species (electron donors).

For the non-equilibrium multi-ion electrolyte, the net current flows through the measuring circuit equal to the sum of individual current induced by various redox couples. Considering Ohm's law, the measured potential at the electrode interface can be calculated as

$$E = R_I \sum_{j=1}^{m} i_{\mathrm{net}_j} \tag{30}$$

where R_I is the potentiometer input resistance (Ω), and i_{net_j} is the individual current induced by redox couple *j* (A).

The individual current of each redox couple can be calculated by the Butler-Volmer equation, which is expressed as the currents from both oxidation (positive sign) and reduction (negative sign) reactions.

https://doi.org/10.5194/hess-2022-31
Preprint. Discussion started: 10 March 2022

Hydrology and Earth System Sciences
Discussions

$$i_{\text{net}_j} = i_{0_j}\left\{\exp\left[-\alpha_j \frac{n_j F}{RT}\left(E - E_{\text{eq}_j}\right)\right] - \exp\left[(1-\alpha_j)\frac{n_j F}{RT}\left(E - E_{\text{eq}_j}\right)\right]\right\} \quad (31)$$

In some theoretical researches, n_j is ignored (Shinagawa et al., 2015), and Eq. 31 is written as

$$i_{\text{net}_j} = i_{0_j}\left\{\exp\left[-\frac{\alpha_j F}{RT}\left(E - E_{\text{eq}_j}\right)\right] - \exp\left[\frac{(1-\alpha_j)F}{RT}\left(E - E_{\text{eq}_j}\right)\right]\right\} \quad (32)$$

where i_{0_j} is the exchange current of redox couple j (A), α_j is the transfer coefficient of redox couple j (-), also known as cathodic transfer coefficient, F is the Faraday constant ($F = 96,484$ C mol^{-1}), R is the gas constant ($R = 8.314$ J mol^{-1} K^{-1}), T is the temperature ($T = 298.15$ K), and E_{eq_j} is the equilibrium potential of redox couple j (V). It can be calculated based on the Nernst equation (Eq. S.6) in Section S.1 (Supplement).

The exchange current represents the balanced Faradaic activity at equilibrium condition. The specific derivation and explanation for exchange current are presented in Section S.1 (Supplement).

$$i_{0_j} = k_{0_j}^{\text{el}} C_{\text{Red}_j}^{\alpha} C_{\text{Ox}_j}^{1-\alpha} n_j F A \quad (33)$$

where $k_{0_j}^{\text{el}}$ is the standard rate constant of redox couple j (m s^{-1}), C_{Red_j} and C_{Ox_j} are concentrations of reduced and oxidized species (mol L^{-1}), and A is the electrode surface area (m^2).

3 Case study

The case study presented here is inspired by an SAT facility, the Shafdan site, Israel, where dynamic water fluxes reach the capillary fringe. The Shafdan's SAT includes six infiltration basins, where each basin is around 2×10^5 m^2 and divided into 9-14 sub-basins (ponds) for alternating flooding (Goren et al., 2014). The SAT basin for treated wastewater (TWW) degradation mainly consists of sandy soil (Goren et al., 2014). The TWW is intermittently discharged into the SAT infiltration basins, creating an alternating oxic and anoxic environment to facilitate contaminant degradation in the subsurface. We assume the capillary fringe suffers an intermittent discharge cycle of 2 flooding days and 4 drying days with a water flux of 9 cm d^{-2} (Fig. S1(a), Supplement). The chemical species types and concentrations in the TWW are presented in Table S.1 (Supplement).

https://doi.org/10.5194/hess-2022-31
Preprint. Discussion started: 10 March 2022


Hydrology and Earth System Sciences
Discussions

The simulation is conducted on a 90cm vertical capillary fringe with 1cm numerical elements, where the groundwater table fluctuates across the vertical soil resulting from TWW discharge. The TWW discharge scenario, including water flux, species concentrations, and gas flow, are set as the upper boundary conditions, while the vertical drainage across the lower boundary of the soil profile depends on the position of groundwater level (Hopmans and Stricker, 1989). The biochemical simulation keeps running with intermittent TWW discharge (i.e., 2 flooding days and 4 drying days) until the subsurface environment becomes pseudo-stable. Then, the physio-bio-chemical dynamics are coupled with the geophysical model and the lower boundary is selected as the reference point for geophysical simulation.

The coupled model (i.e., physico-bio-chemical and geophysical models) runs for two alternating flooding and drying cycles (i.e. 12 days). The study aims to analyze redox potential and SP associated with redox processes in response to redox contaminant concentrations and reaction rates, and streaming potential in response to water content and flux. On the spatial scale, SP, redox potential, and streaming potential along with soil profile on the 1^{st}, 2^{nd}, 4^{th}, and 6^{th} days are analyzed. The 1^{st} and 4^{th} days represent the flooding and drying days, while the 2^{nd} and 6^{th} days represent the change days (i.e., from flooding to drying days and from drying to flooding days, respectively). Moreover, soil depths of 15cm, 45cm, and 75cm represent the unsaturated (0-30cm), alternating (30-60cm), and saturated (60-90cm) zones that are chosen for temporal scale analyses.

3.1 Biochemical processes

For biochemical cycling, C, N, Mn, Fe, S are chosen as the typical redox-sensitive species, and the main biochemical reactions are shown in Fig. 2.

3.1.1 Primary redox reactions

Biochemical kinetic reactions are generally classified as primary and secondary redox reactions. The organic matter degradation pathways are the primary redox reactions (Wang and van Cappellen, 1996; Thullner et al., 2005). These include DON mineralization, DOC aerobic oxidation, denitrification, Mn(IV), Fe(III) and SO_4^{2-} reduction.

https://doi.org/10.5194/hess-2022-31
Preprint. Discussion started: 10 March 2022

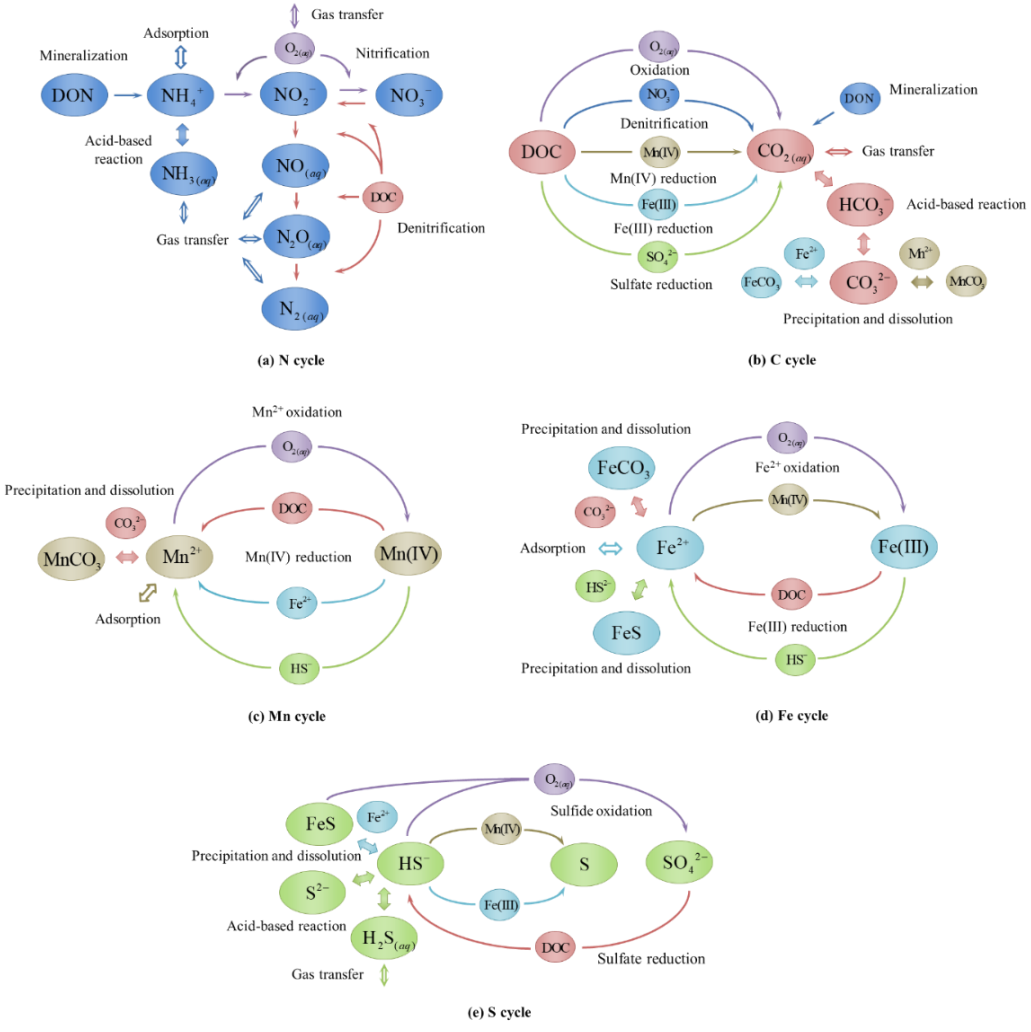

Figure 2 Biochemical cycles of different redox species in the capillary fringe. Panes (a), (b), (c), (d), and (e) represent N, C, Mn, Fe, and S cycles, respectively. DOC and DON are the abbreviations for dissolved organic carbon and nitrogen.

DON mineralization is mainly performed by carbon-oxidizing and denitrifying bacteria in oxic and anoxic environments, respectively (Coelho et al., 2000). For DOC oxidation, the reduced species can be generally listed as O_2, NO_3^-, Mn(IV), Fe(III) and SO_4^{2-} according to the redox sequence. In the oxic environment, DOC tends to be consumed by carbon-oxidizing bacteria through aerobic respiration. When oxygen content becomes less, DOC oxidized by other redox-

https://doi.org/10.5194/hess-2022-31
Preprint. Discussion started: 10 March 2022


Hydrology and Earth System Sciences
Discussions

sensitive species occurs. DOC oxidized by NO_3^- can also be defined as denitrification. NO_3^- is first reduced to NO_2^-, and then NO_2^- is sequentially converted to NO and N_2O. Finally, N_2O is transformed to non-harmful N_2. For DOC oxidized by $Mn(IV)$, $Fe(III)$ and SO_4^{2-}, we define the reaction processes as $Mn(IV)$, $Fe(III)$ and SO_4^{2-} reductions. In DOC oxidation, the existence of higher redox potential species tends to restrict the reaction of the lower one. (Roden, 2008).

The primary redox reactions are solved by multiple-Monod kinetics (Eqs. 7-9), which consider the biomass, biomass and non-competitive inhibition, and substrate concentrations that affect the reaction rates. The kinetic equations and rates for the primary redox reactions are presented in Table 1.

3.1.2 Secondary redox reactions

The reduced species (i.e., NH_4^+, NO_2^-, Mn^{2+}, Fe^{2+} and HS^-) result from primary reactions or other pathways that can be oxidized in an oxidizing environment. These processes are usually referred to as secondary redox reactions. The processes of NH_4^+ and NO_2^- oxidized by O_2 are defined as nitrification and are simulated by multiple-Monod kinetics (Eqs. 7-9). However, for the secondary redox reactions related to Mn^{2+}, Fe^{2+} and HS^-, the kinetic rates are solved by second-order reactions (Eq. 10). This is because these chemical reactions can occur spontaneously and are contributed less by microbial communities (Jaffe et al., 2002; Thullner et al., 2005). The kinetic equations and rates for secondary reactions are described in Table 1.

Table 1 Primary and secondary redox reactions in the biochemical model.

Primary redox reaction	Reaction rate
$RD_x\text{-}NH_2 \xrightarrow[r_{anaer}^{miner}\ NO_3^-]{r_{aer}^{miner}\ O_{2(aq)}} x CH_2O + NH_4^+ + OH^-$	$r_{aer}^{miner} = \mu_{max,\,aer}^{miner} f_{\theta_w} X_{oxid} \left[\frac{k_{b,oxid}}{k_{b,oxid} + f_{\theta_w} X_{oxid}}\right]\left[\frac{DON}{K_{DON,\,aer}^{miner} + DON}\right]\left[\frac{O_2}{K_{O_2}^{miner} + O_2}\right]$ $r_{anaer}^{miner} = \mu_{max,\,anaer}^{miner} f_{\theta_w} X_{denit} \left[\frac{k_{b,denit}}{k_{b,denit} + f_{\theta_w} X_{denit}}\right]\left[\frac{k_{I,O_2}^{miner}}{k_{I,O_2}^{miner} + O_2}\right]\left[\frac{DON}{K_{DON,\,anaer}^{miner} + DON}\right]\left[\frac{NO_3^-}{K_{NO_3^-}^{miner} + NO_3^-}\right]$
$CH_2O + O_{2\,(aq)} \xrightarrow{r^{oxid}} CO_{2\,(aq)} + H_2O$	$r^{oxid} = \mu_{max}^{oxid} f_{\theta_w} X_{oxid} \left[\frac{k_{b,oxid}}{k_{b,oxid} + f_{\theta_w} X_{oxid}}\right]\left[\frac{CH_2O}{K_{CH_2O}^{oxid} + CH_2O}\right]\left[\frac{O_2}{K_{O_2}^{oxid} + O_2}\right]$
$CH_2O + 2NO_3^- \xrightarrow{r^{denit_1}} 2NO_2^- + CO_{2\,(aq)} + H_2O$	$r^{denit_1} = \mu_{max}^{denit_1} f_{\theta_w} X_{denit} \left[\frac{k_{b,denit}}{k_{b,denit} + f_{\theta_w} X_{denit}}\right]\left[\frac{k_{I,O_2}^{denit_1}}{k_{I,O_2}^{denit_1} + O_2}\right]\left[\frac{CH_2O}{K_{CH_2O}^{denit_1} + CH_2O}\right]\left[\frac{NO_3^-}{K_{NO_3^-}^{denit_1} + NO_3^-}\right]$
$CH_2O + 4NO_2^- + 4H^+ \xrightarrow{r^{denit_2}} 4NO_{(aq)} + CO_{2\,(aq)} + 3H_2O$	$r^{denit_2} = \mu_{max}^{denit_2} f_{\theta_w} X_{denit} \left[\frac{k_{b,denit}}{k_{b,denit} + f_{\theta_w} X_{denit}}\right]\left[\frac{k_{I,O_2}^{denit_2}}{k_{I,O_2}^{denit_2} + O_2}\right]\left[\frac{CH_2O}{K_{CH_2O}^{denit_2} + CH_2O}\right]\left[\frac{NO_2^-}{K_{NO_2^-}^{denit_2} + NO_2^-}\right]$
$CH_2O + 4NO_{(aq)} \xrightarrow{r^{denit_3}} 2N_2O_{(aq)} + CO_{2\,(aq)} + H_2O$	$r^{denit_3} = \mu_{max}^{denit_3} f_{\theta_w} X_{denit} \left[\frac{k_{b,denit}}{k_{b,denit} + f_{\theta_w} X_{denit}}\right]\left[\frac{k_{I,O_2}^{denit_3}}{k_{I,O_2}^{denit_3} + O_2}\right]\left[\frac{CH_2O}{K_{CH_2O}^{denit_3} + CH_2O}\right]\left[\frac{NO}{K_{NO}^{denit_3} + NO}\right]$
$CH_2O + 2N_2O_{(aq)} \xrightarrow{r^{denit_4}} 2N_{2\,(aq)} + CO_{2\,(aq)} + H_2O$	$r^{denit_4} = \mu_{max}^{denit_4} f_{\theta_w} X_{denit} \left[\frac{k_{b,denit}}{k_{b,denit} + f_{\theta_w} X_{denit}}\right]\left[\frac{k_{I,O_2}^{denit_4}}{k_{I,O_2}^{denit_4} + O_2}\right]\left[\frac{CH_2O}{K_{CH_2O}^{denit_4} + CH_2O}\right]\left[\frac{N_2O}{K_{N_2O}^{denit_4} + N_2O}\right]$
$CH_2O + 2MnO_{2\,(s)} + 4H^+ \xrightarrow{r^{Mn(IV)}} 2Mn^{2+} + CO_{2\,(aq)} + 3H_2O$	$r^{Mn(IV)} = \mu_{max}^{Mn(IV)} f_{\theta_w} X_{Mn(IV)} \left[\frac{k_{b,Mn(IV)}}{k_{b,Mn(IV)} + f_{\theta_w} X_{Mn(IV)}}\right]\left[\frac{k_{I,O_2}^{Mn(IV)}}{k_{I,O_2}^{Mn(IV)} + O_2}\right]\left[\frac{k_{I,NO_3^-}^{Mn(IV)}}{k_{I,NO_3^-}^{Mn(IV)} + NO_3^-}\right]\left[\frac{CH_2O}{K_{CH_2O}^{Mn(IV)} + CH_2O}\right]\left[\frac{f_\theta MnO_2}{K_{MnO_2}^{Mn(IV)} + f_{\theta_w} MnO_2}\right]$
$CH_2O + 4Fe(OH)_{3\,(s)} + 8H^+ \xrightarrow{r^{Fe(III)}} 4Fe^{2+} + CO_{2\,(aq)} + 11H_2O$	$r^{Fe(III)} = \mu_{max}^{Fe(III)} f_{\theta_w} X_{Fe(III)} \left[\frac{k_{b,Fe(III)}}{k_{b,Fe(III)} + f_{\theta_w} X_{Fe(III)}}\right]\left[\frac{k_{I,O_2}^{Fe(III)}}{k_{I,O_2}^{Fe(III)} + O_2}\right]\left[\frac{k_{I,NO_3^-}^{Fe(III)}}{k_{I,NO_3^-}^{Fe(III)} + NO_3^-}\right]\left[\frac{k_{I,MnO_2}^{Fe(III)}}{k_{I,MnO_2}^{Fe(III)} + f_{\theta_w} MnO_2}\right]\left[\frac{CH_2O}{K_{CH_2O}^{Fe(III)} + CH_2O}\right]\left[\frac{f_\theta Fe(OH)_3}{K_{Fe(OH)_3}^{Fe(III)} + f_{\theta_w} Fe(OH)_3}\right]$
$CH_2O + \frac{1}{2}SO_4^{2-} + \frac{1}{2}H^+ \xrightarrow{r^{sulf}} \frac{1}{2}HS^- + CO_{2\,(aq)} + H_2O$	$r^{sulf} = \mu_{max}^{sulf} f_{\theta_w} X_{sulf} \left[\frac{k_{b,sulf}}{k_{b,sulf} + f_{\theta_w} X_{sulf}}\right]\left[\frac{k_{I,O_2}^{sulf}}{k_{I,O_2}^{sulf} + O_2}\right]\left[\frac{k_{I,NO_3^-}^{sulf}}{k_{I,NO_3^-}^{sulf} + NO_3^-}\right]\left[\frac{k_{I,MnO_2}^{sulf}}{k_{I,MnO_2}^{sulf} + f_{\theta_w} MnO_2}\right]\left[\frac{k_{I,Fe(OH)_3}^{sulf}}{k_{I,Fe(OH)_3}^{sulf} + f_{\theta_w} Fe(OH)_3}\right]\left[\frac{CH_2O}{K_{CH_2O}^{sulf} + CH_2O}\right]\left[\frac{SO_4^{2-}}{K_{SO_4^{2-}}^{sulf} + SO_4^{2-}}\right]$

https://doi.org/10.5194/hess-2022-31
Preprint. Discussion started: 10 March 2022

Hydrology and Earth System Sciences
Discussions
Open Access
EGU

Secondary redox reaction	Reaction rate
$NH_4^+ + \frac{3}{2}O_{2\ (aq)} \xrightarrow{r^{nit_1}} NO_2^- + H_2O + 2H^+$	$r^{nit_1} = \mu_{max}^{nit_1} f_{\theta_w} X_{nit_1} \left[\frac{k_{b,nit_1}}{k_{b,nit_1} + f_{\theta_w} X_{nit_1}}\right]\left[\frac{NH_4^+}{K_{NH_4^+}^{nit_1} + NH_4^+}\right]\left[\frac{O_2}{K_{O_2}^{nit_1} + O_2}\right]$
$NO_2^- + \frac{1}{2}O_{2\ (aq)} \xrightarrow{r^{nit_2}} NO_3^-$	$r^{nit_2} = \mu_{max}^{nit_2} f_{\theta_w} X_{nit_2} \left[\frac{k_{b,nit_2}}{k_{b,nit_2} + f_{\theta_w} X_{nit_2}}\right]\left[\frac{NO_2^-}{K_{NO_2^-}^{nit_2} + NO_2^-}\right]\left[\frac{O_2}{K_{O_2}^{nit_2} + O_2}\right]$
$Mn^{2+} + \frac{1}{2}O_{2\ (aq)} + H_2O \xrightarrow{r^{Mn\_O}} MnO_{2\ (s)} + 2H^+$	$r^{Mn\_O} = k^{Mn\_O}\left[Mn^{2+}\right]\left[O_2\right]$
$Fe^{2+} + \frac{1}{4}O_{2\ (aq)} + \frac{5}{2}H_2O \xrightarrow{r^{Fe\_O}} Fe(OH)_{3\ (s)} + 2H^+$	$r^{Fe\_O} = k^{Fe\_O}\left[Fe^{2+}\right]\left[O_2\right]$
$Fe^{2+} + \frac{1}{2}MnO_{2\ (s)} + 2H_2O \xrightarrow{r^{Fe\_Mn}} Fe(OH)_{3\ (s)} + \frac{1}{2}Mn^{2+} + H^+$	$r^{Fe\_Mn} = k^{Fe\_Mn}\left[Fe^{2+}\right]\left[f_{\theta_w} MnO_2\right]$
$HS^- + 2O_{2\ (aq)} \xrightarrow{r^{S\_O}} SO_4^{2-} + H^+$	$r^{S\_O} = k^{S\_O}\left[HS^-\right]\left[O_2\right]$
$HS^- + MnO_{2\ (s)} + 3H^+ \xrightarrow{r^{S\_Mn}} Mn^{2+} + S_{\ (s)} + 2H_2O$	$r^{S\_Mn} = k^{S\_Mn}\left[HS^-\right]\left[f_{\theta_w} MnO_2\right]$
$HS^- + 2Fe(OH)_{3\ (s)} + 5H^+ \xrightarrow{r^{S\_Fe}} 2Fe^{2+} + S_{\ (s)} + 6H_2O$	$r^{S\_Fe} = k^{S\_Fe}\left[HS^-\right]\left[f_{\theta_w} Fe(OH)_3\right]$
$FeS_{\ (s)} + 2O_{2\ (aq)} \xrightarrow{r^{FeS\_O}} Fe^{2+} + SO_4^{2-}$	$r^{FeS\_O} = k^{FeS\_O}\left[f_{\theta_w} FeS\right]\left[O_2\right]$

1

https://doi.org/10.5194/hess-2022-31
Preprint. Discussion started: 10 March 2022

Hydrology and Earth System Sciences
Discussions
Open Access
EGU

3.1.3 Equilibrium reactions

In addition to primary and secondary redox reactions, there are also equilibrium reactions in the aqueous phase (i.e., complexation and hydrolysis), between aqueous and solid phases (i.e., precipitation and dissolution), between the aqueous phase and the solid surface (i.e., adsorption and desorption), and between aqueous and gas phases (i.e., dissolution and volatilization). The equilibrium constants for aqueous, solid, surface, and gas phases are presented as Eqs. 12, 13, 15, and 18, respectively. The constants for the equilibrium reactions are shown in Table 2.

Table 2 Equilibrium reactions in the biochemical model.

Complexation and hydrolysis	Hydrolysis equilibrium constant
$HCO_3^- \xleftrightarrow{K^h_{HCO_3^-}} CO_3^{2-} + H^+$	$K^h_{HCO_3^-} = \frac{[CO_3^{2-}][H^+]}{[HCO_3^-]}$
$CO_{2\,(aq)} + H_2O \xleftrightarrow{K^h_{H_2CO_3}} CO_3^{2-} + 2H^+$	$K^h_{H_2CO_3} = \frac{[CO_3^{2-}][H^+]^2}{[CO_2]}$
$NH_4^+ \xleftrightarrow{K^h_{NH_4^+}} NH_{3\,(aq)} + H^+$	$K^h_{NH_4^+} = \frac{[NH_3][H^+]}{[NH_4^+]}$
$HS^- \xleftrightarrow{K^h_{HS^-}} S^{2-} + H^+$	$K^h_{HS^-} = \frac{[S^-][H^+]}{[HS^-]}$
$H_2S_{\,(aq)} \xleftrightarrow{K^h_{H_2S}} HS^- + H^+$	$K^h_{H_2S} = \frac{[HS^-][H^+]}{[H_2S]}$
Precipitation and dissolution	**Solubility product constant**
$MnCO_{3\,(s)} \xleftrightarrow{K^{SP}_{MnCO_3}} Mn^{2+} + CO_3^{2-}$	$K^{SP}_{MnCO_3} = [Mn^{2+}][CO_3^{2-}]$
$FeCO_{3\,(s)} \xleftrightarrow{K^{SP}_{FeCO_3}} Fe^{2+} + CO_3^{2-}$	$K^{SP}_{FeCO_3} = [Fe^{2+}][CO_3^{2-}]$
$FeS_{\,(s)} + H^+ \xleftrightarrow{K^{SP}_{FeS}} Fe^{2+} + HS^-$	$K^{SP}_{FeS} = \frac{[Fe^{2+}][HS^-]}{[H^+]}$
$CaCO_{3\,(s)} \xleftrightarrow{K^{SP}_{CaCO_3}} Ca^{2+} + CO_3^{2-}$	$K^{SP}_{CaCO_3} = [Ca^{2+}][CO_3^{2-}]$
$CaSO_{4\,(s)} \xleftrightarrow{K^{SP}_{CaSO_4}} Ca^{2+} + SO_4^{2-}$	$K^{SP}_{CaSO_4} = [Ca^{2+}][SO_4^{2-}]$
$MgCO_{3\,(s)} \xleftrightarrow{K^{SP}_{MgCO_3}} Mg^{2+} + CO_3^{2-}$	$K^{SP}_{MgCO_3} = [Mg^{2+}][CO_3^{2-}]$

https://doi.org/10.5194/hess-2022-31
Preprint. Discussion started: 10 March 2022

Hydrology and Earth System Sciences
Discussions
Open Access
EGU

Adsorption	Surface equilibrium constant
$NH_4^+ + X^- \xleftrightarrow{K^S_{NH_4^+}} NH_4X$	$K^S_{NH_4^+} = \frac{[NH_4X]}{[NH_4^+][X^-]}$
$Fe^{2+} + 2X^- \xleftrightarrow{K^S_{Fe^{2+}}} FeX_2$	$K^S_{Fe^{2+}} = \frac{[FeX_2]}{[Fe^{2+}][X^-]^2}$
$Mn^{2+} + 2X^- \xleftrightarrow{K^S_{Mn^{2+}}} MnX_2$	$K^S_{Mn^{2+}} = \frac{[MnX_2]}{[Mn^{2+}][X^-]^2}$
$Na^+ + X^- \xleftrightarrow{K^S_{Na^+}} NaX$	$K^S_{Na^+} = \frac{[NaX]}{[Na^+][X^-]}$
$K^+ + X^- \xleftrightarrow{K^S_{K^+}} KX$	$K^S_{K^+} = \frac{[KX]}{[K^+][X^-]}$
$Ca^{2+} + 2X^- \xleftrightarrow{K^S_{Ca^{2+}}} CaX_2$	$K^S_{Ca^{2+}} = \frac{[CaX_2]}{[Ca^{2+}][X^-]^2}$
$Mg^{2+} + 2X^- \xleftrightarrow{K^S_{Mg^{2+}}} MgX_2$	$K^S_{Mg^{2+}} = \frac{[MgX_2]}{[Mg^{2+}][X^-]^2}$
Gas dissolution and volatilization	**Henry's law constant**
$CO_{2\ (g)} \xleftrightarrow{K^H_{CO_2}} CO_{2\ (aq)}$	$K^H_{CO_2} = \frac{C_{CO_2}}{P_{CO_2}}$
$NH_{3\ (g)} \xleftrightarrow{K^H_{NH_3}} NH_{3\ (aq)}$	$K^H_{NH_3} = \frac{C_{NH_3}}{P_{NH_3}}$
$NO_{\ (g)} \xleftrightarrow{K^H_{NO}} NO_{\ (aq)}$	$K^H_{NO} = \frac{C_{NO}}{P_{NO}}$
$N_2O_{\ (g)} \xleftrightarrow{K^H_{N_2O}} N_2O_{\ (aq)}$	$K^H_{N_2O} = \frac{C_{N_2O}}{P_{N_2O}}$
$N_{2\ (g)} \xleftrightarrow{K^H_{N_2}} N_{2\ (aq)}$	$K^H_{N_2} = \frac{C_{N_2}}{P_{N_2}}$
$H_2S_{\ (g)} \xleftrightarrow{K^H_{H_2S}} H_2S_{\ (aq)}$	$K^H_{H_2S} = \frac{C_{H_2S}}{P_{H_2S}}$
$O_{2\ (g)} \xleftrightarrow{K^H_{O_2}} O_{2\ (aq)}$	$K^H_{O_2} = \frac{C_{O_2}}{P_{O_2}}$

1

https://doi.org/10.5194/hess-2022-31
Preprint. Discussion started: 10 March 2022


Hydrology and Earth System Sciences
Discussions

3.1.4 Microbial dynamics

In this component of the model, the microbial communities are conceptualized to have 7 types, namely, (i) heterotrophic carbon-oxidizing bacteria; (ii) heterotrophic denitrifying bacteria; (iii) heterotrophic Mn(IV)-reducing bacteria; (iv) heterotrophic Fe(III)-reducing bacteria; (v) heterotrophic sulfate-reducing bacteria (Lensing et al., 1994); (vi) autotrophic ammonia-oxidizing bacteria; and (vii) autotrophic nitrite-oxidizing bacteria. In order to simplify the model, we ignore the direct competition between different types of bacteria. However, carbon-oxidizing bacteria and autotrophic bacteria may indirectly compete for oxygen, while heterotrophic bacteria compete for organic matter for metabolism. The general equation for microbial dynamics is presented as Eq. 14. The character, biochemical process involvement, and microbial dynamics for different bacteria are shown in Table 3.

3.2 Self-potential response

For streaming potential, the physical output parameters (e.g., water pressure head, saturation, and flux) from the physio-bio-chemical model are used as the input data to simulate streaming potential and current density. The simulation can follow the processes in Eq. 23 and Section 2.2.1.

Redox species concentrations and water saturation are used to couple biochemical and redox potential models for redox potential calculation. The redox reaction rates for Fe, Mn, and S are weak because the concentrations of Fe and Mn species are quite low, and the environment is also suitable for sulfate stable existence. Thus, we ignore these species and only consider redox species of O, N, and C for redox potential simulation. Based on the reactions, 7 pairs of redox couples (i.e. H_2O/O_2, NH_4^+/NO_2^-, NO_2^-/NO_3^-, NO/NO_2^-, N_2O/NO, N_2/N_2O, CH_2O/HCO_3^-) are considered in the model. Then, the redox potential can be simulated by the processes in Sections 2.2.2 and S.1 (Supplement). After that, the SP and current density associated with redox processes can also be calculated based on Eqs. 24 and 28.

Based on the simulated processes of source current densities described in the above two paragraphs, the SP signals can be finally calculated as Eq. 22. After that, we can analyze SP signals (including streaming potential and SP associated with redox processes) in response to water content and flux, as well as redox species concentrations and reaction rates, and finally, apply the SP model to practice.

Table 3 Microbial communities in the biochemical model.

Microbial community	Character	Biochemical process	Microbial dynamics
Heterotrophic carbon-oxidizing bacteria	Aerobic heterotrophic bacteria	DOC aerobic oxidation DON mineralization	$\frac{dX_{\text{oxid}}}{dt} = Y_{\text{oxid}}\theta_w r^{\text{oxid}} - X_{\text{oxid}} d_{\text{oxid}}$
Heterotrophic denitrifying bacteria	Anaerobic heterotrophic bacteria	Denitrification DON mineralization	$\frac{dX_{\text{denit}}}{dt} = Y_{\text{denit}}\theta_w (r^{\text{denit}_1} + r^{\text{denit}_2} + r^{\text{denit}_3} + r^{\text{denit}_4}) - X_{\text{denit}} d_{\text{denit}}$
Heterotrophic Mn(IV)-reducing bacteria	Anaerobic heterotrophic bacteria	Mn(IV) reduction	$\frac{dX_{\text{Mn(IV)}}}{dt} = Y_{\text{Mn(IV)}}\theta_w r^{\text{Mn(IV)}} - X_{\text{Mn(IV)}} d_{\text{Mn(IV)}}$
Heterotrophic Fe(III)-reducing bacteria	Anaerobic heterotrophic bacteria	Fe(III) reduction	$\frac{dX_{\text{Fe(III)}}}{dt} = Y_{\text{Fe(III)}}\theta_w r^{\text{Fe(III)}} - X_{\text{Fe(III)}} d_{\text{Fe(III)}}$
Heterotrophic sulfate-reducing bacteria	Anaerobic heterotrophic bacteria	Sulfate reduction	$\frac{dX_{\text{sulf}}}{dt} = Y_{\text{sulf}}\theta_w r^{\text{sulf}} - X_{\text{sulf}} d_{\text{sulf}}$
Autotrophic ammonia-oxidizing bacteria	Aerobic autotrophic bacteria	Ammonium transformation to nitrite	$\frac{dX_{\text{nit}_1}}{dt} = Y_{\text{nit}_1}\theta_w r^{\text{nit}_1} - X_{\text{nit}_1} d_{\text{nit}_1}$
Autotrophic nitrite-oxidizing bacteria	Aerobic autotrophic bacteria	Nitrite transformation to nitrate	$\frac{dX_{\text{nit}_2}}{dt} = Y_{\text{nit}_2}\theta_w r^{\text{nit}_2} - X_{\text{nit}_2} d_{\text{nit}_2}$

https://doi.org/10.5194/hess-2022-31
Preprint. Discussion started: 10 March 2022


Hydrology and Earth System Sciences
Discussions

3.3 Data calibration and verification

The experimental data is first used for model calibration and verification.

3.3.1 Experiment setup

The experimental data was courtesy of Zhang and Furman (2021), and the experiment was conducted in a soil column of 91cm operating for 29 days. The studied soil (98.47% sand, 0.66% clay, and 0.87% silt) was sampled from the SAT site, Yavne 2, Shafdan, Israel (Sopilniak et al., 2017). The schematic of soil biochemical and geophysical experiments are shown in Fig. 3. The water level was kept at around 49cm with solution injected from the top every 3 or 4 days. The water flux was 1.2-2.0cm/h, and the duration lasted for 3-5h in each flooding event. The water input flux and chemical species concentrations are shown in Fig. S.1(b) and Table S.1 (Supplement), respectively. To control the water table was stable at around 49cm, water discharge was conducted simultaneously at the bottom of the soil column.

Soil water matric potential was measured every 15 min by self-made tensiometers (porous ceramic cup (#230, SDEC®), PVC tubes (ACF0007, Tygon®), and a transducer (MPX2100DP, Freescale®)). A sensor measured the oxygen volume percentage at the headspace (KE-25, Figaro®). The chemical species concentrations (i.e., DOC, DON, NH_4^+, and NO_3^-) used for model calibration were measured around 6 hours before water flooding and drainage events. The tensiometers were inserted at the soil depths of 1cm, 11cm, … 81cm. However, the chemical species were measured only at the depths of 41cm, 51cm, … 91cm, as the soil water was hard to extract from the unsaturated soil above 41cm. The extracted pore water (55ml) was sampled with Rhizon CSS samplers (19.21.24F, Rhizosphere®) and filtered through a 0.22μm filter unit (PVDF membrane, Millex®GV) before the measurement. In the pore water, dissolved inorganic nitrogen species (NH_4^+, NO_2^- and NO_3^-) were measured by the spectrophotometer (GENESYS 10S UV-Vis, Thermo Fisher Scientific®). DOC and total dissolved nitrogen were measured by the TOC-V (Shimadzu®). DON was attained by the concentrations of total dissolved nitrogen subtracting dissolved inorganic nitrogen (the sum of NH_4^+, NO_2^- and NO_3^-).

https://doi.org/10.5194/hess-2022-31
Preprint. Discussion started: 10 March 2022

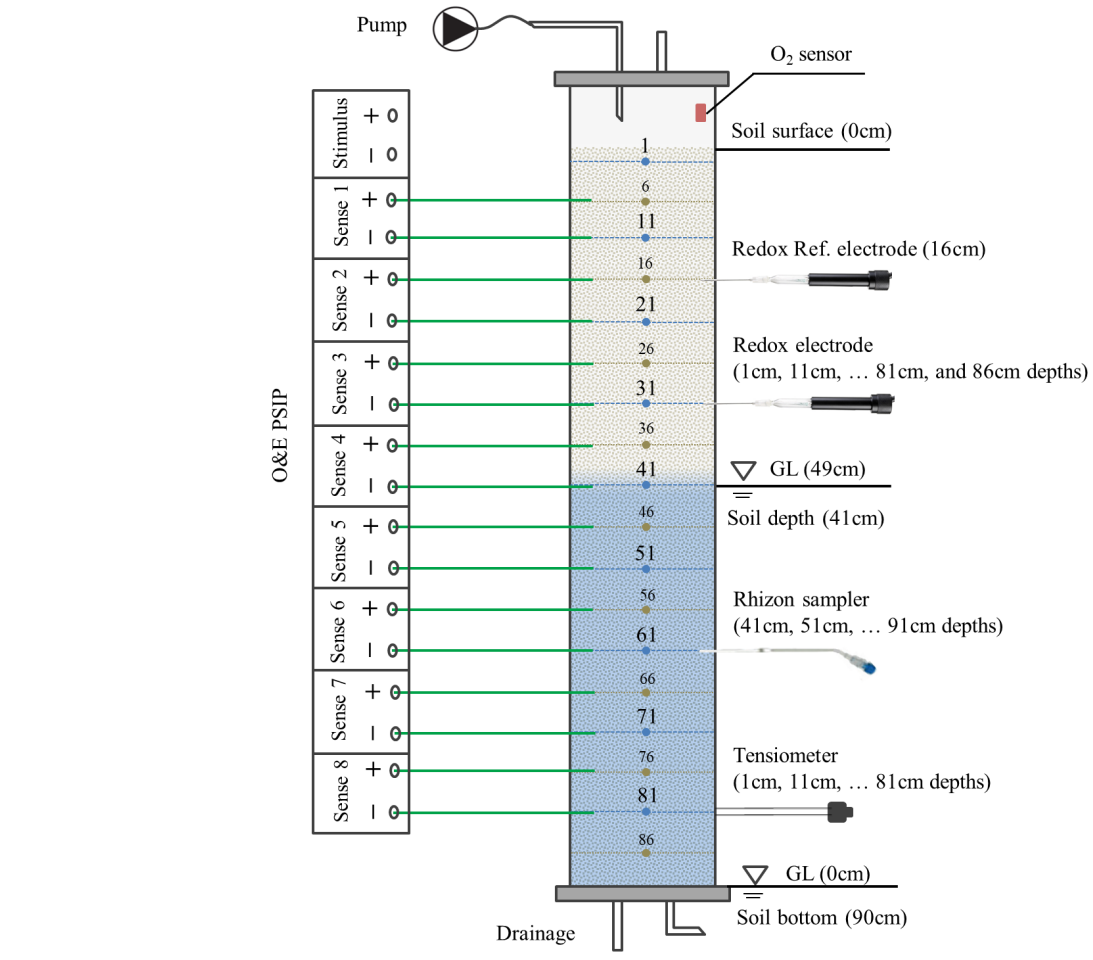

Figure 3 Schematic of soil biochemical and geophysical experiments.

Redox electrodes (#461, ecoTech®) were inserted at the soil depths of 1cm, 11cm, …81cm, and 86cm to measure the redox potential every 15 min with the reference electrode (#4622, ecoTech®) inserted at 16cm depth. The SP differences were measured every 5cm along the soil column by a portable spectral induce polarization (PSIP) equipment (Ontash & Ermac®) twice a day. The stimulus electrodes were disconnected from the soil column. Two sets of measurements were implemented. The first set was to measure the SP differences of 6-11cm, 16-21cm, …76-81cm soil layers with 8 couples of potential electrodes, while the second set was to measure the data of 11-16cm, 21-26cm, …71-76cm soil layers with 7 pairs of potential electrodes.

https://doi.org/10.5194/hess-2022-31
Preprint. Discussion started: 10 March 2022


Hydrology and Earth System Sciences
Discussions

3.3.2 Parameter collection

As such, a model contains several 10s of parameters, part of the parameters were calibrated, while the majority of parameters were collected from the literature. In cases, the parameters recommended by the HP1 software (Šimůnek et al., 2009; Parkhurst and Appelo, 2013) were adopted. The main parameters for soil physical properties, multiple-Monod kinetics and microbial dynamics, second-order reactions, and various equilibrium reactions are shown in Tables S.2-S.5 (Supplement), while parameters for SP modeling are listed in Tables S.6 and S.7 (Supplement) and described in Section 2.2.

The soil physical and biochemical state variables (e.g., solute concentrations, water, and gas pressure) first measured in the 4th day were used as initial conditions. The simulation ran for 25 days. The upper boundary conditions were set as variable water flux, gas flow, and solute concentrations from the top. The lower boundary conditions were set as variable water flux that equals the surface flux and the solute-free drainage.

3.3.3 Calibrated and verified results

In physico-bio-chemical processes, water pressure, DOC, DON, ammonium, and nitrate concentration data at 41 cm and 61 cm depth was used to calibrate the model, while the 51cm and 71cm data was used for verification. In geophysical response, the redox potential of 41cm and SP difference of 26-31cm were used for model calibration, while those of 81cm and 51-56cm were used for model verification. The Nash-Sutcliffe efficiency coefficient (NSE) was used to evaluate the simulation results of contaminant concentrations, and the formulation is presented as follows.

$$E_{ns} = 1 - \frac{\sum (C_s - C_m)^2}{\sum (C_m - \bar{C}_m)^2} \tag{34}$$

where C_s, C_m and $\bar{C}_m$ are the simulated, measured, and average measured values, respectively (mmol L^{-1}), and E_{ns} is the Nash-Sutcliffe efficiency coefficient ($0 \le E_{ns} \le 1$). Thus, when E_{ns} is close to 1, the simulated values are close to the measured values, and vice versa.

(1) Physico-bio-chemical model

The physicio-bio-chemical model calibration and verification results are shown in Fig. S.2 (Supplement). The measured and simulated water pressure values and different contaminant

https://doi.org/10.5194/hess-2022-31
Preprint. Discussion started: 10 March 2022

Hydrology and Earth System Sciences
Discussions

concentrations can generally match well at different soil depths. NSEs are also relatively higher for different species.

The abnormal increasing trend for measured water pressure at 41cm is due to the gas bubble mixed in the tensiometer, which causes measurement errors. Additionally, an accident of water leakage occurred on the 22nd day, the water pressure of measured data presents abnormal trends at different depths after that day.

For chemical species concentrations, the NSE values of DOC and DON at 51cm and 71cm are relatively lower. Because the insoluble SOM decomposition is ignored in the model, some simulated concentrations of DON and DOC are a little lower than the measured data. Moreover, there are no initial concentrations above 41cm, affecting the simulated results at the adjacent soil depth. Thus, NSEs of ammonium and nitrate concentrations are also a little lower at 41cm depth.

(2) Self-potential model

The geophysical calibrated and verified results are shown in Fig. 4. We can see that the changing trends of measured and simulated values for redox potential are matched well.

As for the SP difference, the simulated values are relatively stable in the unsaturated area (i.e. 26-31cm), while the measured values slightly fluctuate around the simulated results. In the experiment, the soil is heterogeneous even at the same layer, but the electrodes are usually in contact with limited soil. In the unsaturated area, the water flow can easily affect soil water character and their contact with electrodes. Thus, the SP differences show slight fluctuation. In numerical modeling, the soil is considered to be homogeneous at the same layer. Oxygen concentration is stable and dominates the SP signature in unsaturated soil, so SP differences of simulated results are relatively stable on the temporal scale.

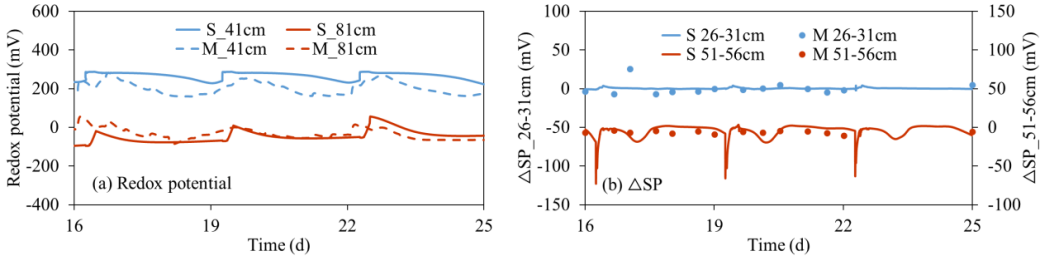

Figure 4 Measured and simulated values of redox potential and SP differences for model calibration and verification. Panes (a) and (b) represent calibrated and verified results for redox potential and SP differences, respectively. Capitals M and S represent measured and simulated values.

https://doi.org/10.5194/hess-2022-31
Preprint. Discussion started: 10 March 2022

Hydrology and Earth System Sciences
Discussions

In the saturated zone (i.e., 51-56cm), the measured values are relatively stable, but simulated values tend to fluctuate periodically. In the experiment, the electrodes are fully in contact with the aqueous phase in the saturated soil, so the measurement errors caused by the heterogeneous soil environment are not as obvious as those in unsaturated soil. Moreover, the SP data was not measured during water infiltrates when the chemical species, reaction rates, and water saturation can be further affected by water flow. However, the periodical water recharge and discharge will cause the transient oxic environment and dynamic biochemical changes in the saturated area, so the SP signals show transient fluctuation trends in the simulated values.

4 Results and discussion

4.1 Spatial analyses

4.1.1 Redox potential

SP and Redox potential in response to redox species concentrations and reaction rates along soil depth are shown in Fig. 5. SP associated with redox processes is not shown in the figure because it is visually hard to distinguish from SP, caused by the little contribution from streaming potential. In the following, we mainly focus on redox potential analyses as SP presents almost opposite trends to redox potential. Redox potential is higher and stable above 40cm due to the oxic environment, but declines below 40cm because of the gradual decrease in oxygen concentration (Fig. 5(b)).

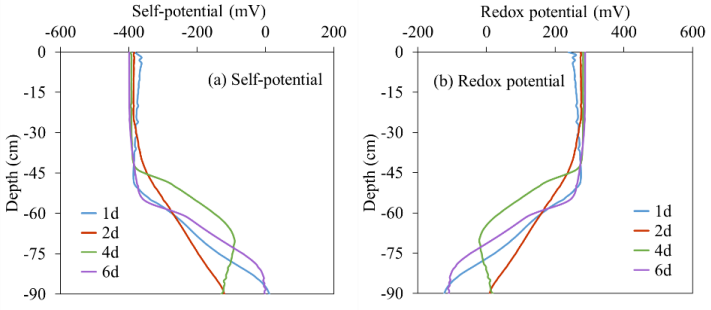

https://doi.org/10.5194/hess-2022-31
Preprint. Discussion started: 10 March 2022

Hydrology and Earth System Sciences
Discussions

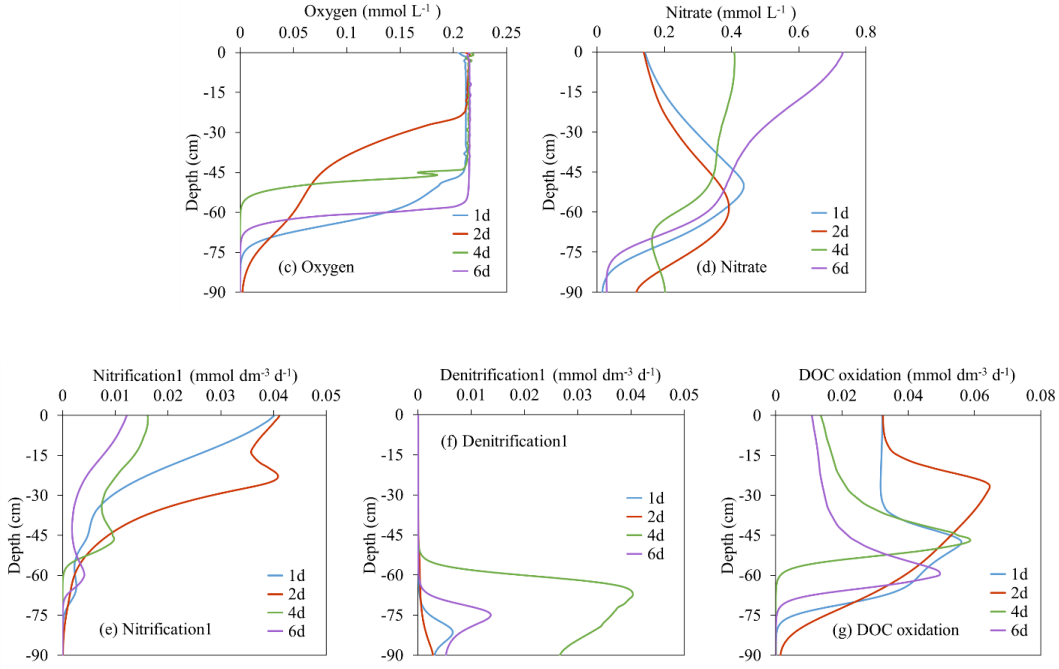

Figure 5 Self-potential and redox potential in response to redox species concentrations and reaction rates along with the soil profile. Panes (a) and (b) indicate SP and redox potential. Panes (c) and (d) refer to oxygen and nitrate concentrations. Panes (c), (d), and (e) represent the reaction rates for ammonium transformation to nitrate (i.e. nitrification 1), nitrate conversion to nitrite (i.e. denitrification 1), and DOC aerobic oxidation, respectively.

Redox potential is mostly affected by oxygen and nitrate concentrations (Fig. 5(c) and (d)). In the unsaturated area (upper layer), the changing trends of redox potential are similar to those of oxygen concentrations for the 4 typical days. However, the trends are mainly affected by nitrate concentrations in the saturated zone (lower layer), where oxygen concentrations are low. In the alternating area (middle layer), the redox potential is dominated by both oxygen and nitrate concentrations, and the trends are relatively complex.

Generally, nitrification and DOC aerobic oxidation are stronger in a higher redox environment (unsaturated and alternating soil) (Fig. 5(e) and (f)), while denitrification is higher in a lower redox environment (saturated soil) (Fig. 5(g)). The redox potential values of 100-350mV, -50-50mV, and 50-250mV are generally considered as the optimal ranges for nitrification, denitrification, and DOC aerobic oxidation in wastewater treatment (Gerardi, 2016; Marin et al., 2016). The most suitable redox environment for nitrification is above 50cm based on the optimal

https://doi.org/10.5194/hess-2022-31
Preprint. Discussion started: 10 March 2022

Hydrology and Earth System Sciences
Discussions

ranges. From 50cm to 75cm, redox potential for different days tends to be gradually lower than 100mV in sequence. Below 75cm, the redox potential values for the 4 days are all less than 100mV. Meanwhile, the nitrification rates show gradual downward trends along with soil depth. The reaction rates above 50cm layer are relatively higher, but the rates from 50cm to75cm tend to be lower, and the rates are close to 0 below 75cm. Moreover, the higher denitrification rates in deeper soil on different days also correspond to the optimal redox potential range (-50-50mV). As for DOC aerobic oxidation, the optimal redox potential range is slightly lower than that of nitrification. This causes DOC oxidation rates not always to be the highest in the upper soil, and the relatively higher reaction rates can also extend to relatively deeper soil. Thus, the stronger reaction rates tend to shift from unsaturated to upper saturated soil for the 4 typical days, corresponding to the suitable redox potential range (50-250mV).

4.1.2 Streaming potential

The streaming potential in response to water content and flux along with soil depth is shown in Fig. 6. The magnitude can be around 100 mV for redox potential, while the magnitude for streaming potential is only around 0.01 mV. Thus, the streaming potential can be neglected in the high biochemical dynamic and low water flux environment. However, to analyze the relationships between steaming potential with water content and flux, we present the simulated results and briefly describe them. Along with soil depth, the negative values of streaming potential become less remarkable, and the changing trends are mainly affected by water content and flux. At the same depth, the intensive water flux and low water content tend to result in more remarkable negative values.

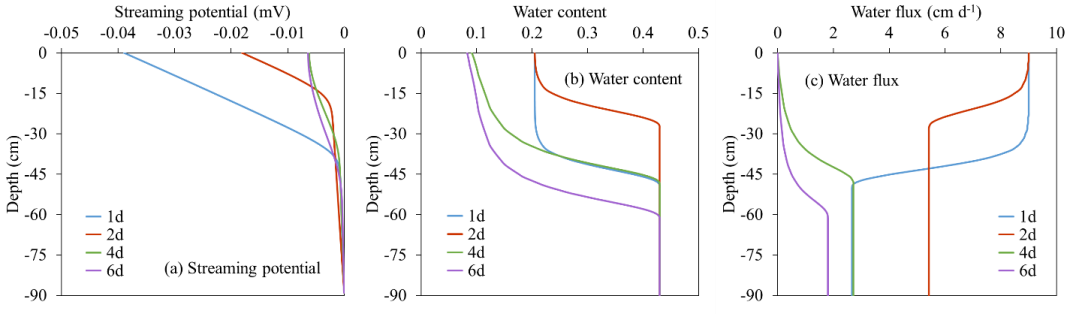

Figure 6 Streaming potential in response to water content and flux along with the soil profile. Panes (a), (b), and (c) represents streaming potential, water content, and water flux, respectively.

https://doi.org/10.5194/hess-2022-31
Preprint. Discussion started: 10 March 2022

Hydrology and Earth System Sciences
Discussions

4.2 Temporal analyses

4.2.1 Redox potential

SP and redox potential in response to redox species concentrations and reaction rates in time series are shown in Fig. 7. In the unsaturated zone (15cm), the fluctuating nitrate concentration shows little impact on redox potential. Oxygen concentration and redox potential are relatively high and stable and result in high nitrification and DOC oxidation rates. However, the reaction rates increase in flooding days (i.e. the 0-2nd day and 6-8th day) but decrease in drying days (i.e. the 2-6th day and 8-12th day), affected by water content changes resulting from dynamic water flow.

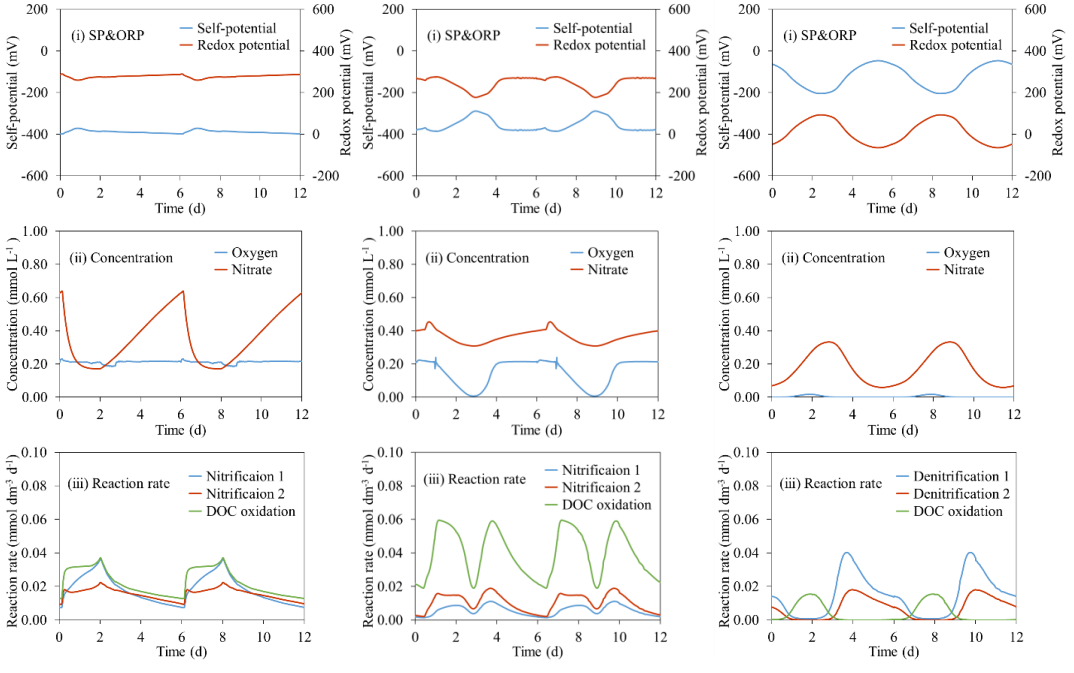

(a) 15cm (b) 45cm (c) 75cm

Figure 7 Self-potential and redox potential in response to redox species concentrations and reaction rates in time series. Panes (a), (b), and (c) represent 15cm, 45cm, and 75cm depths respectively. Sub-panes (i), (ii), and (iii) represent SP&ORP, redox species concentrations, and reaction rates at the corresponding depths. ORP means redox potential. Nitrification 2 indicates nitrite transformation to nitrate, and denitrification 2 refers to nitrite conversion to nitric oxide. Denitrification in 15cm and 45cm and nitrification in 75cm are not shown as the reaction rates are too low and can be ignored compared to other reactions.

https://doi.org/10.5194/hess-2022-31
Preprint. Discussion started: 10 March 2022


Hydrology and Earth System Sciences
Discussions

In the alternating zone (45cm), redox potential fluctuates with water table changes (caused by the alternating flooding and drying days) and shows positive relationships with oxygen and nitrate concentrations. However, redox reaction rates (i.e., nitrification and DOC aerobic oxidation) present abnormal negative relationships with redox potential on the 0-1st day, 4-7th days, and 10-12th days. This is because the reaction rates are affected by the water content changes in partially saturated soil on these days (Fig. 8(b)). Denitrification rates are quite low in both unsaturated and alternating zones, so they are not shown in the figure and are not specifically discussed in the text.

In the saturated zone (75cm), the oxygen content is low. Generally, redox potential presents positive relationships with nitrate concentration and DOC aerobic oxidation rate but a negative relationship with denitrification rate. As the infiltrating water from flooding facilitates oxygen transport to deeper soil, DOC oxidation shows periodical higher rates (around the 2nd and 8th days) in the saturated area. The redox potential is also within the optimal value for DOC oxidation. However, a similar situation does not occur to nitrification as the redox potential is below the optimal values for nitrification. On the other hand, the denitrification rate tends to be higher around the 4th and 10th days corresponding to the optimal redox potential range (-50-50mV), but the rate is close to 0 when the DOC oxidation rate periodical increases.

Based on the spatial and temporal analyses, the simulated SP and redox potential can better reflect redox species concentrations (i.e., oxygen and nitrate in the oxic and anoxic environment, respectively) and reaction rates (nitrification, denitrification, and DOC aerobic oxidation). Thus, the model can be used to assess redox-sensitive contaminant distribution and degradation spatially and temporally.

4.2.2 Streaming potential

Streaming potential in response to water content and flux in time series are presented in Fig. 8. The streaming potential is mainly affected by water flux. At the same depth, the more intensive water flow tends to cause more obvious negative values in streaming potential. Moreover, the negative values in the upper soil are more remarkable than those in the lower soil. However, the water content effect on streaming potential is not obvious in temporal representation as the water flux impact is more significant and the temporal changes of water content are less remarkable than those on the spatial scale. Thus, the streaming potential signature can be used to estimate the effectiveness of soil moisture and water leakage detection (also see the spatial analyses section).

https://doi.org/10.5194/hess-2022-31
Preprint. Discussion started: 10 March 2022

Hydrology and Earth System Sciences
Discussions

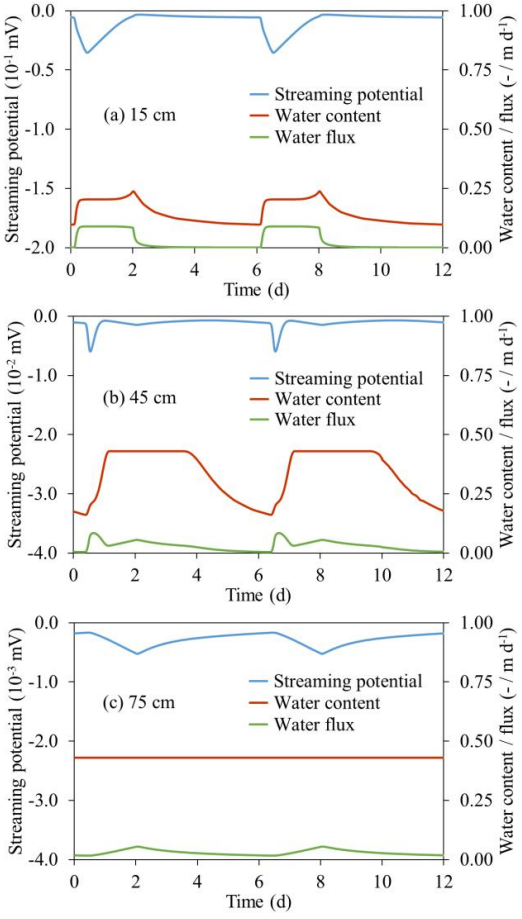

Figure 8 Streaming potential in response to water content and flux in time series. Panes (a), (b), and (c) represent 15cm, 45cm, and 75cm depths respectively.

5 Summary and conclusions

In this research, we couple the physio-bio-chemical and geophysical models and simulate the SP signature in response to carbon and nitrogen transformation and transport under dynamic TWW discharge in an SAT basin.

The physio-bio-chemical model can better simulate the physical and biochemical dynamics in the subsurface, such as water pressure and carbon and nitrogen contaminants. The coupled models show that SP signature is mostly contributed by redox processes in the case study. The redox potential and SP signature can reflect the redox species concentrations, including oxygen and nitrate in the oxic and anoxic environment, respectively. Moreover, the signals are also

https://doi.org/10.5194/hess-2022-31
Preprint. Discussion started: 10 March 2022


Hydrology and Earth System Sciences
Discussions

sensitive to redox reaction rates, i.e., nitrification, denitrification, and DOC aerobic oxidation. The higher reaction rates for different redox processes correspond to their optimal redox potential ranges. The streaming potential contributes little to SP signature and is affected by water flux and content. Thus, the model can be used to instruct or assess redox-sensitive contaminant monitoring and soil moisture and water leakage detection in case studies.

However, studies related to redox potential solved by the Butler-Volmer equation are rare, and we cannot compare the results with other studies for further model verification. Additionally, the values for model parameters are usually broad, and in cases are based on very different models, so the parameters must be repeatedly verified when applying the model to other cases. Confronting this model with additional data, at the laboratory and field scales, is needed. However, such data is relatively rare.

Appendices

Table A.1 Superscript symbols.

Superscript	Description
miner	Mineralization
oxid	DOC aerobic oxidation
$denit_1$	Nitrate reduction
$denit_2$	Nitrite reduction
$denit_3$	Nitric oxide reduction
$denit_4$	Nitrous oxide reduction
Mn(IV)	Mn(IV) reduction
Fe(III)	Fe(III) reduction
sulf	Sulfate reduction
nit_1	Ammonium oxidation
nit_2	Nitrite oxidation
Mn_O	Ferrous oxidized by oxygen
Fe_O	Bivalent manganese oxidized by oxygen

https://doi.org/10.5194/hess-2022-31
Preprint. Discussion started: 10 March 2022


Hydrology and Earth System Sciences
Discussions

Fe_Mn	Bivalent manganese oxidized by Mn(IV)
S_O	Sulfide oxidized by oxygen
S_Mn	Sulfide oxidized by Mn(IV)
S_Fe	Sulfide oxidized by Fe(III)
FeS_O	Ferrous sulfide oxidized by oxygen

Table A.2 Subscript symbols.

Subscript	Description
aer	Aerobic mineralization
anaer	Anaerobic mineralization
oxid	Heterotrophic carbon-oxidizing bacteria
denit	Heterotrophic denitrifying bacteria
Mn(IV)	Mn(IV)-reducing bacteria
Fe(III)	Fe(III)-reducing bacteria
sulf	Sulfate-reducing bacteria
nit_1	Autotrophic ammonia-oxidizing bacteria
nit_2	Autotrophic nitrite-oxidizing bacteria

Code availability

The code for soil physical model is the built-in code in Hydrus-1D. The code for soil biochemical and geophysical models is the programming code conducted in HP1 and Matlab. Any requests for access to the code can be addressed to the corresponding authors.

Data availability

The data for parameters, experiment, and case study is available in the supplement.

Author contributions

https://doi.org/10.5194/hess-2022-31
Preprint. Discussion started: 10 March 2022

XL built and calibrated the models, analyzed the simulated results, and wrote the paper. ZZ provided the experimental data and instructed the experiment section writing. AF instructed model development and revised the paper. All authors read and checked the paper.

Competing interests

The authors declare that they have no conflict of interest.

Acknowledgements

This research is partially supported by the Gerald Schwartz & Heather Reisman Foundation, University of Waterloo-Technion; partially financed by the German-Israeli Water Technology Cooperation Program (project number: 02WIL1451A/WT1601), German Federal Ministry of Education and Research (BMBF), and Israeli Ministry of Science, Technology and Space (MOST).

References

Abbas, M., Jardani, A., Ahmed, A.S., Revil, A., Brigaud, L., Bégassat, P., Dupont, J.-P., 2017. Redox potential distribution of an organic-rich contaminated site obtained by the inversion of self-potential data. Journal of Hydrology 554, 111–127.

Allègre, V., Lehmann, F., Ackerer, P., Jouniaux, L., Sailhac, P., 2012. A 1-D modelling of streaming potential dependence on water content during drainage experiment in sand. Geophysical Journal International 189, 285–295.

Archie, G.E., 1942. The electrical resistivity log as an aid in determining some reservoir characteristics. Transactions of the AIME 146, 54–62.

Arora, T., Linde, N., Revil, A., Castermant, J., 2007. Non-intrusive characterization of the redox potential of landfill leachate plumes from self-potential data. Journal of Contaminant Hydrology 92, 274–292.

Bear, J., 1972. Dynamics of fluids in porous media. American Elsevier Publishing Company, New York.

Bolève, A., Janod, F., Revil, A., Lafon, A., Fry, J.-J., 2011. Localization and quantification of leakages in dams using time-lapse self-potential measurements associated with salt tracer injection. Journal of Hydrology 403, 242–252.

https://doi.org/10.5194/hess-2022-31
Preprint. Discussion started: 10 March 2022


Hydrology and Earth System Sciences
Discussions

Bolève, A., Revil, A., Janod, F., Mattiuzzo, J.L., Jardani, A., 2007. Forward modeling and validation of a new formulation to compute self-potential signals associated with ground water flow. Hydrology and Earth System Sciences 11, 1661–1671.

Butler, J.A.V., 1932. The mechanism of overvoltage and its relation to the combination of hydrogen atoms at metal electrodes. Transactions of the Faraday Society 28, 379–382.

Butler, J.A.V., 1924a. Studies in heterogeneous equilibria. Part II.—The kinetic interpretation of the nernst theory of electromotive force. Transactions of the Faraday Society 19, 729–733.

Butler, J.A.V., 1924b. Studies in heterogeneous equilibria. Part III. A kinetic theory of reversible oxidation potentials at inert electrodes. Transactions of the Faraday Society 19, 734–739.

Castermant, J., Mendonça, C.A., Revil, A., Trolard, F., Bourrié, G., Linde, N., 2008. Redox potential distribution inferred from self-potential measurements associated with the corrosion of a burden metallic body. Geophysical Prospecting 56, 269–282.

Coelho, M.A.Z., Russo, C., Araujo, O.Q.F., 2000. Optimization of a sequencing batch reactor for biological nitrogen removal. Water Research 34, 2809–2817.

Cui, Y., Zhu, X., Wei, W., Liu, J., Tong, T., 2017. Dynamic imaging of metallic contamination plume based on self-potential data. Transactions of Nonferrous Metals Society of China 27, 1822–1830.

DesRoches, A.J., Butler, K.E., 2016. Monitoring and modelling of pumping-induced self-potentials for transmissivity estimation within a heterogeneous confined aquifer. Geophysical Journal International 207, 1722–1738.

Dickinson, E.J., Wain, A.J., 2020. The Butler-Volmer equation in electrochemical theory: Origins, value, and practical application. Journal of Electroanalytical Chemistry 872, 114145.

Duy Thanh, L., Jougnot, D., van Do, P., van Nghia A, N., 2019. A physically based model for the electrical conductivity of water-saturated porous media. Geophysical Journal International 219, 866–876.

Erdey-Grúz, T., Volmer, M., 1930. Zur theorie der wasserstoff überspannung. Zeitschrift für Physikalische Chemie 150, 203–213.

Fernandez, P.M., Bloem, E., Binley, A., Philippe, R.S., French, H.K., 2019. Monitoring redox sensitive conditions at the groundwater interface using electrical resistivity and self-potential. Journal of Contaminant Hydrology 226, 103517.

https://doi.org/10.5194/hess-2022-31
Preprint. Discussion started: 10 March 2022


Hydrology and Earth System Sciences
Discussions

Forté, S.A., Bentley, L.R., 2013. Mapping degrading hydrocarbon plumes with self potentials: Investigation on causative mechanisms using field and modeling data. Journal of Environmental and Engineering Geophysics 18, 27–42.

Gerardi, M.H., 2016. An Operator's Guide to Biological Nutrient Removal (BNR) in the Activated Sludge Process. Chemical Publishing Company.

Goren, O., Burg, A., Gavrieli, I., Negev, I., Guttman, J., Kraitzer, T., Kloppmann, W., Lazar, B., 2014. Biogeochemical processes in infiltration basins and their impact on the recharging effluent, the soil aquifer treatment (SAT) system of the Shafdan plant, Israel. Applied Geochemistry 48, 58–69.

Hamelers, H.V., Ter Heijne, A., Stein, N., Rozendal, R.A., Buisman, C.J., 2011. Butler–Volmer–Monod model for describing bio-anode polarization curves. Bioresource Technology 102, 381–387.

Hopmans, J.W., Stricker, J.N.M., 1989. Stochastic analysis of soil water regime in a watershed. Journal of Hydrology 105, 57–84.

Hu, K., Jougnot, D., Huang, Q., Looms, M.C., Linde, N., 2020. Advancing quantitative understanding of self-potential signatures in the critical zone through long-term monitoring. Journal of Hydrology 585, 124771.

Jaffe, P.R., Wang, S., Kallin, P.L., Smith, S.L., 2002. The dynamics of arsenic in saturated porous media: fate and transport modeling for deep aquatic sediments, wetland sediments, and groundwater environments. The Geochemical Society, Special Publication 7, 379–397.

Jardani, A., Revil, A., Boleve, A., Crespy, A., Dupont, J.P., Barrash, W., Malama, B., 2007. Tomography of the Darcy velocity from self-potential measurements. Geophysical Research Letters 34, L24403.

Jin, X., Bandodkar, A.J., Fratus, M., Asadpour, R., Rogers, J.A., Alam, M.A., 2020. Modeling, design guidelines, and detection limits of self-powered enzymatic biofuel cell-based sensors. Biosensors and Bioelectronics 168, 112493.

Jouniaux, L., Allègre, V., Toussaint, R., Zyserman, F., 2020. Saturation dependence of the streaming potential coefficient. Seismoelectric Exploration: Theory, Experiments, and Applications 73–100.

Jouniaux, L., Maineult, A., Naudet, V., Pessel, M., Sailhac, P., 2009. Review of self-potential methods in hydrogeophysics. Comptes Rendus Geoscience 341, 928–936.

https://doi.org/10.5194/hess-2022-31
Preprint. Discussion started: 10 March 2022


Hydrology and Earth System Sciences
Discussions

Kindred, J.S., Celia, M.A., 1989. Contaminant transport and biodegradation: 2. Conceptual model and test simulations. Water Resources Research 25, 1149–1159.

Lensing, H.J., Vogt, M., Herrling, B., 1994. Modeling of biologically mediated redox processes in the subsurface. Journal of Hydrology 159, 125–143.

Li, D., 2004. Electrokinetics in microfluidics. Elsevier.

Linde, N., Revil, A., 2007. Inverting self-potential data for redox potentials of contaminant plumes. Geophysical Research Letters 34, L14302.

Lyklema, J., 1995. Fundamentals of interface and colloid science. Volume II: Solid-liquid interfaces. Academic Press.

Marin, J.C.A., Caravelli, A.H., Zaritzky, N.E., 2016. Nitrification and aerobic denitrification in anoxic–aerobic sequencing batch reactor. Bioresource Technology 200, 380–387.

Mboh, C.M., Huisman, J.A., Zimmermann, E., Vereecken, H., 2012. Coupled hydrogeophysical inversion of streaming potential signals for unsaturated soil hydraulic properties. Vadose Zone Journal 11, vzj2011. 0115.

Meyer, D., Prien, R.D., Dellwig, O., Waniek, J.J., Schulz–Bull, D.E., 2014. Electrode measurements of the oxidation reduction potential in the Gotland Deep using a moored profiling instrumentation. Estuarine, Coastal and Shelf Science 141, 26–36.

Millington, R.J., Quirk, J.P., 1961. Permeability of porous solids. Transactions of the Faraday Society 57, 1200–1207.

Möckel, D., Staude, E., Dal-Cin, M., Darcovich, K., Guiver, M., 1998. Tangential flow streaming potential measurements: hydrodynamic cell characterization and zeta potentials of carboxylated polysulfone membranes. Journal of Membrane Science 145, 211–222.

Molz, F.J., Widdowson, M.A., Benefield, L.D., 1986. Simulation of microbial growth dynamics coupled to nutrient and oxygen transport in porous media. Water Resources Research 22, 1207–1216.

Monod, J., 1949. The growth of bacterial cultures. Annual Reviews in Microbiology 3, 371–394.

Mualem, Y., 1976. A new model for predicting the hydraulic conductivity of unsaturated porous media. Water Resources Research 12, 513–522.

Oliveti, I., Cardarelli, E., 2017. 2D approach for modelling self-potential anomalies: application to synthetic and real data. Bollettino di Geofisica Teorica ed Applicata 58.

https://doi.org/10.5194/hess-2022-31
Preprint. Discussion started: 10 March 2022


Hydrology and Earth System Sciences
Discussions

Parkhurst, D.L., Appelo, C.A.J., 2013. Description of input and examples for PHREEQC version 3: a computer program for speciation, batch-reaction, one-dimensional transport, and inverse geochemical calculations. No. 6-A43. US Geological Survey.

Peiffer, S., Klemm, O., Pecher, K., Hollerung, R., 1992. Redox measurements in aqueous solutions – A theoretical approach to data interpretation, based on electrode kinetics. Journal of Contaminant Hydrology 10, 1–18.

Picioreanu, C., Head, I.M., Katuri, K.P., van Loosdrecht, M.C., Scott, K., 2007. A computational model for biofilm-based microbial fuel cells. Water Research 41, 2921–2940.

Revil, A., 2013. Effective conductivity and permittivity of unsaturated porous materials in the frequency range 1mHz-1GHz. Water Resources Research 49, 306–327.

Revil, A., Koch, K., Holliger, K., 2012. Is it the grain size or the characteristic pore size that controls the induced polarization relaxation time of clean sands and sandstones? Water Resources Research 48, W05602.

Revil, A., Mendonça, C.A., Atekwana, E.A., Kulessa, B., Hubbard, S.S., Bohlen, K.J., 2010. Understanding biogeobatteries: Where geophysics meets microbiology. Journal of Geophysical Research 115, G00G02.

Revil, A., Trolard, F., Bourrie, G., Castermant, J., Jardani, A., Mendonça, C.A., 2009. Ionic contribution to the self-potential signals associated with a redox front. Journal of Contaminant Hydrology 109, 27–39.

Roden, E.E., 2008. Microbiological controls on geochemical kinetics 1: fundamentals and case study on microbial Fe (III) oxide reduction, in: Kinetics of Water-Rock Interaction. Springer, pp. 335–415.

Santos, F.A.M., Almeida, E.P., Castro, R., Nolasco, R., Mendes-Victor, L., 2002. A hydrogeological investigation using EM34 and SP surveys. Earth, Planets and Space 54, 655–662.

Schüring, J., Schulz, H.D., Fischer, W.R., Böttcher, J., Duijnisveld, W.H., 2000. Redox: fundamentals, processes and applications. Springer-Verlag Berlin Heidelberg.

Segel, I.H., 1975. Enzyme kinetics: behavior and analysis of rapid equilibrium and steady state enzyme systems. John Wiley & Sons, New York.

https://doi.org/10.5194/hess-2022-31
Preprint. Discussion started: 10 March 2022


Hydrology and Earth System Sciences
Discussions

Shinagawa, T., Garcia-Esparza, A.T., Takanabe, K., 2015. Insight on Tafel slopes from a microkinetic analysis of aqueous electrocatalysis for energy conversion. Scientific Reports 5, 13801.

Sill, W.R., 1983. Self-potential modeling from primary flows. Geophysics 48, 76–86.

Šimůnek, J., Šejna, M., Saito, H., Sakai, M., Van Genuchten, M.Th., 2009. The HYDRUS-1D software package for simulating the one-dimensional movement of water, heat, and multiple solutes in variably-saturated media. University of California, University of California Riverside, USA.

Soldi, M., Guarracino, L., Jougnot, D., 2020. An effective excess charge model to describe hysteresis effects on streaming potential. Journal of Hydrology 588, 124949.

Sopilniak, A., Elkayam, R., Lev, O., 2017. Nitrification in a soil-aquifer treatment system: comparison of potential nitrification and concentration profiles in the vadose zone. Environmental Science: Processes & Impacts 19, 1571–1582.

Soueid Ahmed, A., Jardani, A., Revil, A., Dupont, J.-P., 2016. Joint inversion of hydraulic head and self-potential data associated with harmonic pumping tests. Water Resources Research 52, 6769–6791.

Soueid Ahmed, A., Revil, A., Bolève, A., Steck, B., Vergniault, C., Courivaud, J.R., Jougnot, D., Abbas, M., 2020. Determination of the permeability of seepage flow paths in dams from self-potential measurements. Engineering Geology 268, 105514.

Soueid Ahmed, A., Revil, A., Steck, B., Vergniault, C., Jardani, A., Vinceslas, G., 2019. Self-potential signals associated with localized leaks in embankment dams and dikes. Engineering Geology 253, 229–239.

Tanaka, N., Tamamushi, R., 1964. Kinetic parameters of electrode reactions. Electrochimica Acta 9, 963–989.

Thullner, M., van Cappellen, P., Regnier, P., 2005. Modeling the impact of microbial activity on redox dynamics in porous media. Geochimica et Cosmochimica Acta 69, 5005–5019.

van Genuchten, M.T., 1980. A closed-form equation for predicting the hydraulic conductivity of unsaturated soils. Soil Science Society of America Journal 44, 892–898.

Wang, Y., van Cappellen, P., 1996. A multicomponent reactive transport model of early diagenesis: Application to redox cycling in coastal marine sediments. Geochimica et Cosmochimica Acta 60, 2993–3014.

https://doi.org/10.5194/hess-2022-31
Preprint. Discussion started: 10 March 2022

Yu, R.F., Liaw, S.L., Chang, C.N., Lu, H.J., Cheng, W.Y., 1997. Monitoring and control using on-line ORP on the continuous-flow activated sludge batch reactor system. Water Science and Technology 35, 57–66.

Zhang, Z., Furman, A., 2021. Redox dynamics at a dynamic capillary fringe for nitrogen cycling in a sandy column. Journal of Hydrology 603, 126899.

Zhao, L., Li, J., Battaglia, F., He, Z., 2016. Investigation of multiphysics in tubular microbial fuel cells by coupled computational fluid dynamics with multi-order Butler–Volmer reactions. Chemical Engineering Journal 296, 377–385.